Systematic E2 screening reveals a UBE2D-RNF138-CtIP axis promoting DNA repair

Christine K Schmidt[#1], **Yaron Galanty**[#1,5], **Matylda Sczaniecka-Clift**[1], **Julia Coates**[1], **Satpal Jhujh**[1], **Mukerrem Demir**[1], **Matthew Cornwell**[1], **Petra Beli**[3], and **Stephen P Jackson**[1,2,5]

[1]The Wellcome Trust/Cancer Research UK Gurdon Institute and Department of Biochemistry, University of Cambridge, CB2 1QN Cambridge, UK

[2]The Wellcome Trust Sanger Institute, Hinxton, CB10 1SA Cambridge, UK

[3]Institute of Molecular Biology (IMB), 55128 Mainz, Germany

[#] These authors contributed equally to this work.

Abstract

Ubiquitylation is crucial for proper cellular responses to DNA double-strand breaks (DSBs). If unrepaired, these highly cytotoxic lesions cause genome instability, tumourigenesis, neurodegeneration or premature ageing. Here, we conduct a comprehensive, multilayered screen to systematically profile all human ubiquitin E2-enzymes for impacts on cellular DSB responses. Applying a widely applicable approach, we use an exemplary E2 family, UBE2Ds, to identify ubiquitylation-cascade components downstream of E2s. Thus, we uncover the nuclear E3-ligase RNF138 as a key homologous recombination (HR)-promoting factor that functions with UBE2Ds in cells. Mechanistically, UBE2Ds and RNF138 accumulate at DNA-damage sites and act at early resection stages by promoting CtIP ubiquitylation and accrual. This work supplies insights into regulation of DSB repair by HR. Moreover, it provides a rich information resource on E2s that can be exploited by follow-on studies.

In response to DSBs, cells mediate a complex, highly regulated DNA-damage response (DDR) to sense DNA lesions and arrest cell-cycle progression to allow DNA repair, or initiate apoptosis1,2. One principal DSB-repair mechanism is non-homologous end-joining (NHEJ), which is active throughout the cell-cycle and occurs through two pathways: classical NHEJ and alternative/microhomology-mediated end-joining (MMEJ)3. The other, homologous recombination (HR), requires a sister chromatid as template and is limited to S/G2 cell-cycle phases2. Key to initiating HR is DNA-end resection promoted by CtIP (RBBP8) recruitment to DSB sites2,4,5, yielding single-stranded DNA (ssDNA) that is

rapidly bound by RPA and subsequently replaced by RAD51, leading to strand invasion and ensuing HR processes2. Precisely how CtIP and early HR events are regulated, however, is not known.

Among the earliest DDR events is activation of the protein kinases ATM, ATR and DNA-PKcs6. Activated ATM phosphorylates histone H2AX (H2AFX) to yield γH2AX at DSBs, which in turn recruits numerous DDR modulators into ionizing-radiation induced foci (IRIF)1,2,7. Recently, ubiquitylation has emerged as a key DDR regulator8. Mediated by two E1 activating, ~40 E2 conjugating and >600 E3 ligating enzymes, posttranslational modification by ubiquitin modulates the stability, localization, activity or interaction properties of proteins9,10. E2s, previously regarded as mere basic ubiquitylation components, have recently emerged as key ubiquitylation mediators. E2-E3 pairs exist in various combinations, controlling the switch between ubiquitin-chain initiation and elongation, and determining ubiquitylation processivity and linkage specificity11,12. Despite the above, few systematic analyses of human E2s or E3s have been conducted, although recent proteomic approaches have identified hundreds of DDR-regulated ubiquitylation substrates13, suggesting that E2s and many E3s with DDR roles await discovery.

Here, using a three-module, siRNA-based, semi-automated analysis pipeline, we systematically interrogate E2s for DSB-response functions in human cells. In addition to identifying various E2s with previously non-established DDR functions, we show how such data can be used to identify E2-E3-substrate ubiquitylation pathways. Specifically, by applying data-mining and phenotypic-mimicry approaches, we identify the ubiquitin-E3-ligase RNF138 as a DDR factor that cooperates with UBE2Ds to promote HR by stimulating CtIP ubiquitylation and accrual at DSB sites.

Results

Systematic multi-module screen for DDR E2s

To identify E2 DDR components, we performed loss-of-function screens in U2OS cells with siRNA pools targeting 37 E2s, control siRNA (siCTRL) and validated siRNAs against known DDR factors (Supplementary Table 1). We evaluated siRNA-treatments of all known ubiquitin-E2s and the two NEDD8-E2s, UBE2M and UBE2F. To obtain comprehensive DDR "fingerprints" we multiplexed the screen into three modules.

Module 1 evaluated impacts of E2 depletions on IRIF kinetics for DDR factors/markers by semi-automated, quantitative high-content, high-throughput (HC/HT) microscopy (Fig. 1a, and Supplementary Fig. 1a-b). 96-well plates containing duplicates for each siE2 were irradiated or not, fixed and assessed for γH2AX IRIF (a DNA-damage marker), 53BP1 (TP53BP1) whose IRIF require ubiquitin8, and conjugated ubiquitin (FK2 antibody). Validating the screening pipeline, depleting the ubiquitin-E3s RNF8 and RNF168, or depleting UBE2N that has known DDR connections, strongly impaired FK2 and 53BP1 but not γH2AX IRIF (Fig. 1b)8. Notably, siRNAs targeting 19 E2s diminished induction of FK2 IRIF 30 minutes after IR, to <60% of siCTRL cells; and surprisingly given established links between conjugated ubiquitin and 53BP1 IRIF8, without markedly affecting 53BP1 or

γH2AX foci (Fig. 1b, Supplementary Fig. 1c, *PubChem BioAssays* and Discussion). Depleting UBE2D, -R, -J, -Q1, -Q2, UBE2O or -K, reduced induction of FK2 IRIF to <25% of siCTRL, while siUBE2D3 reduced FK2 IRIF induction by >97% (Fig. 1b-c; siUBE2D3 is highlighted because we subsequently found that it depleted all UBE2D family members). Collectively, these results suggested that many E2s impact on DDR IRIF, particularly FK2-ubiquitin foci (Fig. 1b-c, Supplementary Fig. 1c and *PubChem BioAssays*).

Module 2 evaluated HR and mutagenic end-joining (mutEJ) by the traffic-light-reporter (TLR) system in U2OS cells14,15 (Fig. 2a; as HR operates only in S/G2, data were corrected to flow-cytometry S/G2 values). Positive controls of ATM inhibition or CtIP depletion significantly decreased HR4,16, while DNA-PK inhibition decreased mutEJ, likely via DNA-PK retention at DSBs impeding access of other factors. Furthermore, the proteasome inhibitor MG132 drastically impaired HR, highlighting the importance of ubiquitylation in HR17. In agreement with this, we found that depleting many E2s markedly inhibited HR (Fig. 2b, Supplementary Table 2 and *PubChem BioAssays*). Furthermore, depleting several E2s, most notably UBE2O and -R2, strongly impaired mutEJ (Fig. 2c, and Supplementary Table 2).

Module 3 measured DDR signalling triggered by IR that generates DSBs throughout the cell-cycle), or camptothecin (CPT), a topoisomerase I poison that yields S-phase DSBs, which are repaired by HR and activate ATR. DDR readouts employed were CHK1 (CHEK1) phosphorylated on Ser-345 (pCHK1, a marker for ATR activation), RPA2 phosphorylated on Ser-4 and Ser-8 (pRPA2, a resection marker) and KAP1 (TRIM28) phosphorylated on S824 (pKAP1, mainly ATM-dependent). γH2AX and Cyclin A (CCAN2) were used as markers for DNA-damage induction and cells in S/G2, respectively (Fig. 3a, Supplementary Fig. 2a-d). As expected4, siCtIP reduced pRPA2 and pCHK1 but not γH2AX or pKAP1 following camptothecin-treatment (Fig. 3b and Supplementary Fig. 2a4). BRCA1 depletion decreased pCHK1 induction and, consistent with recent findings indicating that BRCA1 functions mainly downstream of resection initiation18–22, strongly reduced HR (7.91% ±4.45% SD of siCTRL, n=4) but not camptothecin-induced pRPA2 (Fig. 3b and Supplementary Fig. 2a4).

Strikingly, many siE2s affected camptothecin- and IR-induced DDR signalling, with pCHK1 effects following camptothecin generally correlating with reduced pRPA2 (Fig. 3b-c). Of the 37 E2 depletions, many produced >40% reductions in pRPA2 following camptothecin (20 E2s), pCHK1 following camptothecin (21 E2s) or pCHK1 after IR (17 E2s; Fig. 3d; see examples in Fig. 3e). Decreased camptothecin-induced pCHK1 sometimes correlated with impaired pKAP1 and γH2AX induction, possibly reflecting lower S-phase indices (Supplementary Fig. 2a and 2c). Notably, however, 10 siE2s affected all three DDR readouts (Fig. 3d) but not IR-induced pKAP1 and γH2AX (Fig. 3c, Supplementary Fig. 2a1-4, and 2d), indicating that the targeted E2s likely possess DDR functions. These included UBE2N, -O, -V2, -D, -R, -L and -J family members, plus UBE2T and -W linked to the Fanconi anemia (FA) DNA-repair pathway23,24. These results thus highlighted potential roles of many E2s in ATR signalling, consistent with ubiquitylation promoting ATR activation25. By contrast, the main mark affected by siUBE2S or siBIRC6 was pKAP1 (both after

camptothecin or IR-treatment; Fig. 3c, 3e, Supplementary Fig. 2a3-4 and 2d), suggesting these E2s may promote ATM signalling.

Validating DDR functions for selected E2s

To help interpret screen readouts, we represented them in a Circos plot (Fig. 4a). Here, siE2s are plotted clockwise in order of decreasing DDR impact (segment colours and breadths reflect cumulative impacts based on module readouts) and siE2s scoring in the top 25% of all readouts are connected by ribbons to the respective colour-coded readout (further details in Fig. 4a). Thus, it is clear that many siE2 treatments affected HR, with various siE2s also impairing FK2 IRIF. By contrast, mutEJ effects were less pronounced, possibly reflecting the lower complexity of end-joining than HR.

To validate the value of our screening data for future studies, we selected E2 families where at least one family member had 3 connecting Circos plot ribbons (Fig. 4a). Excluding UBE2N and -V1, due to their defined DDR functions[8], this group comprised UBE2D, -R, -J and -L members, and UBE2O. Importantly, these 11 siE2s efficiently depleted their targets and, apart from UBE2Ds, no marked cross-depletions were detected (Supplementary Fig. 3 and 4a). By contrast, several siRNAs designed to target a particular UBE2D significantly co-depleted other UBE2Ds (Supplementary Fig. 4a), reflecting their high sequence homology at the mRNA (77-86% coding-sequence identity) and protein levels (Supplementary Fig. 4b). Indeed, we noted that siRNAs targeting UBE2D3 efficiently depleted all UBE2Ds. Similarly, an siRNA designed to target UBE2D2 depleted both UBE2D2 and -D3 and had some effect on UBE2D1 (Supplementary Fig. 4a). While some siUBE2Ds may have unique DDR functions, based on their high degree of sequence homology, it seems likely that they have largely overlapping functions. To avoid potential redundancy issues of UBE2D proteins and strengthen screening data in follow-up experiments, we established an siRNA mixture (siALL-Ds) that efficiently depleted all UBE2Ds (Supplementary Fig. 4c-d). Importantly, when we tested the 11 siRNAs with strongest DDR impacts for potential effects on RAD51, a key HR factor and a common "off-target" for many siRNAs[26], none caused a pronounced reduction in RAD51 (Supplementary Fig. 4e).

We next explored DDR functions for selected E2s by live-imaging of cells expressing GFP-tagged E2s. This revealed that various UBE2R, -L and -D family members displayed both nuclear and cytoplasmic localizations, and were rapidly recruited to DSBs induced by laser micro-irradiation (Fig. 4b; recruitments were weak and detected best between 5 and 30 minutes). By contrast, UBE2O, -J1 and -J2 were largely cytoplasmic and not detected at laser tracts. Thus, >70% (8 of 11) of the selected E2s and 100% of the nuclear ones (UBE2R1, -R2, -L3, -L6, -D1, -D2, -D3 and -D4) accumulated at DSB sites (previously, only UBE2N, -A and -B were shown to do this[27,28]; note that, although overexpressed UBE2J1, -J2 and UBE2O were preferentially cytoplasmic and were not chosen for further analysis, they may impact on the DDR indirectly, or function directly in the DDR requiring associated factors for nuclear localization). We then examined the eight selected DNA-damage-recruited E2s functionally by assessing their impact on proliferation/cell growth after IR-treatment. This revealed that depleting UBE2R1, -R2, -L3 or -L6 with at least two independent siRNAs caused IR hyper-sensitisation, in some cases comparable to siATM

(Fig. 4c). This was also so for co-depleting UBE2Ds. Collectively, these results supported there being important DDR functions for UBE2R1, -R2, -L3, -L6, and -Ds.

DNA-end resection links UBE2Ds to RNF138

Due to their strong phenotypes in multiple screen readouts, we focused subsequent studies on the UBE2D family, co-depleting them with siALL-Ds. In line with our pRPA2 data, depleting UBE2Ds strongly decreased camptothecin-induced formation of ssDNA and nuclear RPA2 foci (to avoid potential cell cycle effects, these analyses focused on γH2AX-positive S phase cells; Fig. 5a). Similar RPA2 foci and ssDNA formation defects were also observed upon MG132 treatment (Supplementary Fig. 5a), consistent with previous reports following intermediate[29] but not extreme[17] IR doses. From these and preceding data on HR and DDR-signalling, we concluded that UBE2Ds function upstream of ssDNA formation to promote ATR signalling and DSB repair by HR.

To explore the mechanism for these effects, we endeavoured to identify the UBE2D partner E3(s). Thus, we selected UBE2D-interacting E3s retrieved from several databases (UniProtKB, MINT, STRING and I2D). To reduce the E3 hits (96, 109, 106 and 99 for UBE2D1, -D2, -D3 and -D4, respectively; 121 unique hits in total), we prioritised E3s previously identified as potential ATM/ATR targets[30]. TRIP12, STUB1 (CHIP), RAD18 and BRCA1 were not selected due to their established DDR phenotypes not being consistent with UBE2Ds-depletion[1,8,31–34]. In particular, BRCA1 depletion did not markedly affect camptothecin-induced pRPA or ssDNA formation in our assays (Fig. 3b and data not shown). Strikingly, when we investigated the resulting six E3s in a semi-automated screen, only RNF138 (RING finger protein 138) depletion substantially impaired ssDNA formation (Fig. 5b). Furthermore, like UBE2Ds-depletion, RNF138 depletion with two independent siRNAs (Supplementary Fig. 5b) markedly reduced RPA2 and ssDNA camptothecin-induced foci (Fig. 5c). Moreover, depleting UBE2Ds and RNF138 simultaneously did not lead to additive effects in BrdU-based ssDNA detection assays (Supplementary Fig. 5c). These results thereby highlighted RNF138 as a DDR factor and potential functional partner of UBE2Ds.

RNF138 and UBE2Ds affect similar DDR processes

RNF138 is a ubiquitin-E3 ligase, highly conserved in higher eukaryotes, containing a RING-domain, three zinc fingers (ZNFs) and a ubiquitin-interacting motif (UIM; Fig. 6a)[35,36]. Live imaging of cells transiently expressing wild-type (WT) GFP-RNF138 (endogenous RNF138 depleted) revealed that it rapidly accumulated at laser tracks (within 5 minutes) and persisted for >1 hour (Fig. 6b). Notably, UBE2D depletion or ATM, ATR or DNA-PK inhibition did not appreciably affect RNF138 accrual or retention at DSBs (Supplementary Fig. 6a and data not shown). By contrast, upon MG132 treatment, initial RNF138 recruitment was weaker, while its retention 25 minutes after micro-irradiation was significantly impaired (Fig. 6b), implicating ubiquitylation events in promoting RNF138 retention at DSB sites. Accordingly, deleting its UIM or mutating the RING-domain (RM; C18/C21A) strongly impaired RNF138 retention (Fig. 6b). The most striking phenotype occurred upon deleting the ZNFs, which – in addition to causing a more predominant localisation in the cytoplasm – severely reduced both RNF138 accrual and retention at DSB

sites (Fig. 6b). Consistent with ZNFs often binding to nucleic acids, wild-type RNF138 but not RNF138 ZNFs bound to streptavidin beads coated with biotinylated DNA (Fig. 6c). Collectively, these data supported a model wherein the ZNFs promote RNF138 recruitment by mediating contacts with exposed DNA at damage sites, and that ubiquitylation events – generated by RNF138 and/or other ubiquitin-E2-E3 pairs – are required for effective RNF138 retention.

Together with the database interaction linkages, the similar impacts of UBE2Ds- and RNF138-depletions on resection suggested that they functionally cooperate. Furthermore, RNF138 depletion mimicked UBE2D1-4 depletion, reducing FK2 and BRCA1 IRIF without markedly influencing 53BP1 or γH2AX IRIF (Fig. 6d-e, and Supplementary Fig. 6b-c). Although a previous report connected UBE2D3 with BRCA137, significant differences in phenotypes between depleting UBE2Ds or BRCA1 in resection (Module 3, Fig. 3b, 5a and data not shown) suggested that UBE2Ds also act upstream to, and independently of, BRCA1. RNF138 depletion also phenocopied UBE2Ds depletion in every other DDR readout we tested. Thus, RNF138 depletion severely impaired HR and also affected mutEJ (Fig. 6f and Supplementary Fig. 6d; controls as in Fig. 2b-c). Finally, like UBE2Ds (Fig. 4c), RNF138 was required for cellular resistance to IR in clonogenic survival and cell proliferation/growth rate assays (Fig. 6g and Supplementary Fig. 6e). Moreover, depleting UBE2Ds and RNF138 simultaneously did not lead to clear additive effects regarding IR-sensitisation or HR efficiency (Supplementary Fig. 6f-g). We therefore concluded that RNF138 acts directly or indirectly with UBE2Ds to promote DSB resection and repair by HR, as well as potentially influencing mutEJ and other DDR processes.

UBE2Ds and RNF138 promote CtIP DNA-damage accrual and ubiquitylation

Key events leading to DSB resection are accumulation of the MRE11-RAD50-NBS1 (MRN) complex and CtIP at DSBs38. Strikingly, we found that depleting UBE2Ds, or RNF138 with two independent siRNAs, strongly impaired recruitment of endogenous or GFP-CtIP to laser tracks but had no discernible effect on GFP-MRE11 recruitment (Fig. 7a-b rows 1-2 and Supplementary Fig. 7a-b). By contrast, CtIP depletion did not affect RNF138 accrual/retention (Supplementary Fig. 7c). Importantly, the CtIP recruitment defect and the siCtIP-related pRPA2- and pCHK1-induction defects in UBE2Ds-depleted cells (Supplementary Fig. 2b) were partially corrected by stable inducible expression of siALL-Ds resistant wild-type (WT) but not catalytically dead (CD) UBE2D1 (Fig. 7a, rows 3-4, 7c and Supplementary Fig. 7d). Similarly, the CtIP recruitment defect caused by RNF138 depletion was almost entirely corrected in stable cell lines by inducible expression of siRNF138-1 resistant WT-RNF138, but not the RING-domain mutant (RM; Fig. 7b, rows 3-4).

The above results and our previous findings supported a model in which the ubiquitin-ligase activities of both UBE2Ds and RNF138 act downstream of MRE11 recruitment to promote CtIP accumulation at DSBs. In line with this and our previous observation that MG132 inhibited DSB resection and HR, MG132 also impaired CtIP accumulation (Supplementary Fig. 7e). As MG132 blocks RNF8-dependent accumulation of RNF168, 53BP1 and BRCA1 at DSBs8, we tested if DNA-damage accumulation of CtIP was impaired by depleting such proteins. In contrast to the impacts of UBE2Ds- or RNF138-depletion, DNA-damage accrual

of CtIP occurred effectively in cells depleted of RNF8, RNF168 or BRCA1 (Supplementary Fig. 7f-g).

Previous work has established that RNF8, RNF168 and BRCA1 are required for effective FK2 IRIF formation[8,37,39]. As we had found that UBE2Ds and RNF138 promote CtIP recruitment to DSBs as well as FK2 and BRCA1 IRIF, we tested if CtIP was required for IRIF formation by these and other DDR components. Significantly, this revealed that FK2, BRCA1 and 53BP1 IRIF still formed efficiently in CtIP-depleted cells (Supplementary Fig. 8a-c). Taking these data together, we concluded that cellular DDR functions of UBE2Ds and RNF138 relating to resection and CtIP accrual are specific and largely independent of RNF8, RNF168 or BRCA1. Conversely, RNF8, RNF168 and BRCA1 clearly promote FK2 IRIF formation and HR via BRCA1 recruitment[1,2,8] and therefore, operate through mechanisms distinct from the UBE2D-RNF138-CtIP-resection axis.

Further strengthening the links between UBE2Ds, RNF138 and CtIP, we found that UBE2D1 co-immunoprecipitated with both RNF138 and CtIP (Fig. 7d). By contrast, we did not detect interactions between RNF138 or CtIP and UBE2K (Supplementary Fig. 8d), another E2 that markedly impaired FK2 IRIF and pRPA2 induction (Fig. 1b, 3b and 4a). Moreover, in reciprocal experiments, RNF138 immunoprecipitation retrieved both UBE2D1 and CtIP (Fig. 7e and Supplementary Fig. 8e). As expected, the GFP-RNF138 RING mutant (RM) did not efficiently co-immunoprecipitate with UBE2D1. However, it efficiently co-immunoprecipitated with CtIP, suggesting RM-RNF138 was not generally misfolded and retained some functionality (Fig. 7e; note: these studies were done in RNF138-depleted cells). Importantly, we found that both ΔUIM and ΔZNFs RNF138 mutants co-immunoprecipitated with UBE2D1 and CtIP to extents comparable to those of wild-type RNF138 (Fig. 7e), suggesting that these two mutants retained some cellular functions.

To test whether CtIP is ubiquitylated in a UBE2Ds/RNF138-dependent manner, we co-expressed HA-ubiquitin with either GFP or GFP-CtIP in cells, then treated or mock-treated cells with IR. Next, we prepared cell extracts and assessed GFP immunoprecipitates for HA-ubiquitin staining by immunoblotting. This revealed ubiquitylation bands migrating above GFP-CtIP that were induced upon IR (Fig. 7f). Importantly, while we detected endogenous RNF138 in CtIP immunoprecipitates (Fig. 7g-h), RNF138 ubiquitylation was not increased by IR (Supplementary Fig. 8e), supporting the idea that the IR-induced species in CtIP immunoprecipitates represented ubiquitylated CtIP. Supporting our finding that CtIP depletion did not impair FK2 IRIF, ubiquitylated forms of CtIP were almost undetectable by the FK2 antibody (Fig. 7f). Crucially, we found that depleting UBE2Ds or RNF138 abolished IR-induced CtIP ubiquitylation (Fig. 7g-h), suggesting that UBE2Ds/RNF138 might mediate ubiquitylation as a functional pair (note that the increase in ubiquitylation in siALL-Ds- over siCTRL-treated cells in the absence of DNA damage is due to experimental variation rather than biological significance). Supporting this hypothesis, UBE2D1, but not UBE2T – another E2 enzyme that scored highly in our screen – supported RNF138-auto-ubiquitylation in *in vitro* assays (Supplementary Fig. 8f). Furthermore, UBE2D1 mediated *in vitro* ubiquitylation of purified CtIP in an RNF138-dependent manner (Supplementary Fig. 8g). These data thus indicated that UBE2Ds and RNF138 can selectively act as a functional

pair and play important roles early on in the DDR to promote IR-induced CtIP ubiquitylation.

Finally, to gain deeper mechanistic insights into the importance of UBE2Ds-/RNF138-dependent CtIP ubiquitylation for DNA-end resection and CtIP recruitment, we identified 13 ubiquitylated lysines on CtIP by mass spectrometry, immunoprecipitated from irradiated cells (Fig. 8a). One of these lysines does not play a role in CtIP recruitment[40], so was excluded from further analyses. In addition to mutating all 12 potentially relevant lysines to arginines (CtIP 12KR), we generated CtIP mutants with lysine-to-arginine mutations clustered in the N- or C-terminal CtIP regions (CtIP 5KR and 6KR, respectively; Fig. 8a). Immunoprecipitation experiments showed that IR-induced ubiquitylation observed with wild-type CtIP was significantly reduced in the context of these mutants, especially CtIP 12KR and 5KR (Fig. 8b). These results suggested that CtIP-N-terminal ubiquitylation may be important for DNA-end resection and CtIP accrual at DSBs. Furthermore, we found that cells stably expressing siRNA-resistant CtIP 5KR failed to complement camptothecin-induced pRPA2 and pCHK1 in cells depleted of endogenous CtIP (Fig. 8c). Moreover, compared with wild-type CtIP, the 5KR mutant displayed significant laser micro-irradiation recruitment defects, implying that IR-induced CtIP ubiquitylation is important for CtIP accumulation at DSBs (Fig. 8d).

Discussion

Although ubiquitylation affects virtually every aspects of eukaryotic cell biology, defining the precise nature of such events, and the ubiquitylation components mediating them, has been difficult because of technical challenges and the large number of ubiquitylation factors (>1,000 in human cells). Here, we provide a paradigm for how key aspects of ubiquitin biology can be defined through focused, in-depth screens for E2-enzyme functions, leveraging this and other knowledge to define E2-E3-target-protein cascades. Accordingly, we have established UBE2D-family proteins as important DDR enzymes, and identified RNF138 as a resection/HR promoting factor that functionally interacts with UBE2Ds and CtIP. Our data are consistent with a model in which UBE2Ds and RNF138 constitute a functional E2-E3 ubiquitylation axis that, either directly or in co-operation with additional factors, promotes IR-induced CtIP ubiquitylations, including on five key lysines towards the CtIP N-terminus. As CtIP's N-terminus is important for CtIP dimerization, tetramerization, recruitment to DSBs and repair by HR[15,41], we speculate that CtIP ubiquitylation in this region may promote these functions by affecting its multimeric state and/or its interactions with other factors. Alternatively or in addition, IR-induced ubiquitylation could expose a recently identified internal DNA binding motif in CtIP[38] to facilitate its DSB recruitment/functions. UBE2Ds/RNF138 could also generate ubiquitylation moieties recognized by CtIP via its proposed ubiquitin binding function[42]. Our data thereby suggest further mechanistic studies to determine precisely how ubiquitylation of these N-terminal CtIP lysines promotes resection and HR. We note however, that UBE2Ds and RNF138 – either as a functional pair or in combination with other ubiquitylation components – likely target additional proteins to affect other pathways within and beyond the DDR. Indeed, the accompanying paper by Ismail *et al.*[43] establishes that RNF138 mediates ubiquitylation of the DSB repair protein, Ku, promoting Ku removal from DSBs to facilitate CtIP access, resection and HR.

Many additional avenues await exploration through exploiting our E2 screening data. For instance, these studies have highlighted links between various understudied E2 proteins and diverse aspects of the DDR, including DSB repair by HR and mutEJ, IRIF formation and ATM/ATR mediated signalling. For example, we found that depletion of various E2s reduced FK2 IRIF, often without affecting 53BP1 IRIF. Since FK2 antibodies likely recognise many conjugated ubiquitin species, including different chain linkages and/or lengths, we speculate that these ubiquitylation events require multiple E2s, serving as initiators or elongators, and/or ubiquitylating the same protein at multiple sites. Moreover, we speculate that FK2 IRIF reduction upon RNF8/RNF168 depletion may partly reflect the reduction of ubiquitylation events promoting BRCA1 recruitment, thought to further amplify FK2 IRIF[37,39]. In line with this hypothesis, previous studies have reported an uncoupling between FK2 and 53BP1 IRIF[44,45]. Collectively, our results suggest that various ubiquitylation events are required for the accumulation of various DDR proteins at DSBs. We also note that FK2 IRIF reduction in ALL-Ds- or RNF138-depleted cells coincided with reduced BRCA1 IRIF. Thus, it will be interesting to explore additional roles of UBE2Ds and RNF138 distinct from the CtIP ubiquitylation-resection axis defined here. It will also be interesting to further study the complex requirements for RNF138 accrual at DSBs, which may have evolved to ensure optimal spatial and temporal control of DSB processing, their downstream signalling and HR. We speculate that follow-on studies emanating from our E2 screen will be greatly facilitated by the use of orthogonal datasets, generated from other functional screens together with proteomic, mutational and gene-expression resources[13,30,46–48]. Finally, it is noteworthy that such work may have medical applications because small-molecule targeting of DDR-enzymes and ubiquitin system components is providing opportunities for cancer therapies[49,50]. Indeed, our findings highlight how certain ubiquitin E2 enzymes with DDR functions may represent attractive therapeutic targets.

Methods

Cell culture

U2OS, U2OS derived and HEK293 cells were cultured at 37°C in a humidified atmosphere containing 5% CO_2 in Dulbecco's Modified Eagle Medium (DMEM; Sigma-Aldrich) supplemented with 10% (v/v) fetal bovine serum (FBS) from BioSera or – for U2OS cells stably expressing tetracycline repressor (U2OS Trex) and derived inducible stable cell lines – tetracycline negative FBS from PAA Laboratories, 100 U/ml penicillin, and 100 μg/ml streptomycin (Sigma-Aldrich). Additional supplements were used to maintain the following stable cell lines: 0.5 mg/ml G418 (Invitrogen) to select constitutively stably expressing GFP-CtIP4 and GFP-FLAG-MRE11 U2OS cells; 2 μg/ml blasticidin (Invitrogen) for U2OS Trex cells, 2 μg/ml blasticidin (Invitrogen) and 0.2 mg/ml zeocin (Life technologies) for U2OS Trex cells stably expressing inducible GFP or siRNF138-1 resistant GFP-RNF138 (WT and RM), 2 μg/ml blasticidin (Invitrogen) and 0.5 mg/mL G418 (Invitrogen) for U2OS Trex cells stably expressing inducible siALL-Ds resistant UBE2D1 (WT and C85S). 2 μg/ml puromycin (Sigma-Aldrich) for U2OS TLR cells. Doxycycline (Sigma-Aldrich) was added at final concentrations of 0.001 μg/ml, 0.003 μg/ml or 1-2 μg/ml for 24-48 hours to induce

comparable levels of GFP, GFP-D1-CD or GFP-D1-WT/GFP-RNF138-WT/GFP-RNF138 C18/21A expression, respectively.

Generation of stable cell lines

Single cell sorting of polyclonal U2OS cells stably expressing GFP-FLAG-MRE11 or GFP-CtIP lysine to arginine mutants (12KR, 6KR or 5KR) was performed to select clones with homogeneous expression of the GFP-tagged proteins. Monoclonal cell lines stably expressing inducible siRNA resistant GFP-RNF-138 WT, GFP-RNF138 C18/21A, GFP-UBE2D1 WT and GFP-UBE2D1 C85S were established using U2OS Trex (pcDNA6/TR Invitrogen) generated in this work.

siRNA and plasmid transfections

Unless otherwise stated siRNA oligonucleotides were designed using the Dharmacon design center and purchased from MWG Biotech. siRNA transfections were performed using Lipofectamine RNAiMAX (Life Technologies) at a final siRNA concentration of ~60 nM according to the manufacturer's instructions. siRNA transfected cells were assayed 48-72 hours after transfection. For siRNA and DNA co-transfections, plasmid transfections were performed 8 hours after siRNA treatment using FuGENE6 (Roche), FuGENE HD (Roche) or TransIT-LT1 (Mirus Bio) following the manufacturer's guidelines. As a negative control we used siRNA oligonucleotides targeting Luciferase (siCTRL). For a complete list of siRNA sequences used in this study see Supplementary Table 1.

Small molecule inhibition

The following conditions were used for the TLR assays: DNA-PK inhibitor (NU7441, Tocris Bioscience) at 3 μM for 72 hours; proteasome inhibitor MG132 (Merck Biosciences/Calbiochem) at 0.1 μM for 48 hours and ATM inhibitor (KU55933, Tocris Bioscience) at 10 μM for 72 hours. For camptothecin, IR or laser micro-irradiation experiments the following inhibitors were added 1 hour before DDR treatments: MG132 at 20 μM, ATM inhibitor (see above) at 10 μM, ATR inhibitor (ATR-45, The Ohio State University, OSUCCC Medical Chemistry) at 1 μM, DNA-PK inhibitor (see above) at 3 μM.

DNA damage induction using chemical agents, IR and laser micro-irradiation

Camptothecin (Sigma-Aldrich) was added to cells for 1 hour at a final concentration of 1 μM. For IR treatments a Faxitron-CellRad (Faxitron Bioptics, LLC) was used. Localised lines of DNA-damage were induced by laser micro-irradiation, essentially as described previously[53,54]. Briefly, U2OS cells were plated on glass-bottom dishes (Willco-Wells), treated with the indicated siRNAs or drugs, and pre-sensitised with 10 μM BrdU (Sigma-Aldrich) in phenol red-free medium (Invitrogen) for ~48 hours at 37°C. Subsequent exposure to a laser beam was performed using a FluoView 1000 confocal microscope (Olympus) equipped with a 37°C heating stage (Ibidi) and a 405 nm laser diode (6 mW) focused through a 60× UPlanSApo/1.35 oil objective and resulting in a spot size of 0.5-1 μm. 250 ms laser beam exposure times (fast scanning mode) were used at a setting of 0.4 mW output (50 scans) to yield pre-sensitisation-dependent DNA-damage, restricted to laser tracks without detectable cytotoxicity. For experiments involving CtIP, a laser power of

0.20-0.25 mW output was used, which resulted specifically in its recruitment to laser tracks in Cyclin A (CycA)-positive S/G2 but not in CycA-negative G1 cells. Cells were laser micro-irradiated for ~20 minutes and left to recover under standard cell culture conditions for 1-2 hours before fixing and staining.

TLR assays

The Traffic Light Reporter (TLR) comprises a mutant *GFP* gene with a unique recognition site for the endonuclease I-SceI followed by a 2 bp out-of-frame *mCherry* gene. Upon transient expression of I-SceI, repair of the induced DSB generates one of two distinct fluorescent gene products depending on the repair pathway employed: (1) GFP in the case of HR using a transiently transfected exogenous donor, the latter being a truncated GFP functional for the part mutated in the TLR, or (2) mCherry in the case of a 2 bp frameshift induced by mutEJ. Therefore, GFP and mCherry expression can be used as readouts for HR and mutEJ efficiencies, respectively[14]. U2OS TLR cells were treated with the indicated siRNA or inhibitor and 8 hours later co-transfected with expression plasmids containing (1) infrared fluorescent protein (IFP) and I-SceI endonuclease and (2) blue fluorescent protein (BFP) together with the donor sequence. Cells were harvested ~72 hours after siRNA transfection. Four-colour fluorescent flow-cytometry using a BD LSRFortessa™ cell analyser (BD Biosciences) allowed direct measurements of the percentages of GFP[+] (HR) and mCherry[+] (mutEJ) cells. A minimum of 10,000 doubly-transfected (IFP[+] and BFP^{+}) cells were scored for each condition in a minimum of three experiments. Analyses were conducted using FlowJo (TreeStar). For each siRNA treatment, results were normalised to the control, a non-targeting siRNA specific for firefly luciferase (siCTRL), resulting in relative HR and mutEJ percentages for each siE2 pool (Fig. 2b and 2c, respectively, Supplementary Table 2 and *Pubchem BioAssays*). Finally, the HR values for each condition were normalised to the total amount of cells in S and G2 phases obtained using propidium iodide based standard flow-cytometry (see 'Cell-cycle profiling' section below). For a comprehensive overview of the screening data and individual values, see *PubChem BioAssays*.

Automated high-throughput/high-content microscopy for IRIF quantification and BrdU assays

48 hours after siRNA transfection, U2OS cells were seeded into 96 well plates (Cell Carrier, Perkin Elmer, 15,000 cells/well). The following day, cells were irradiated or directly processed to retrieve non-treated reference plates. Plates were fixed at the indicated time points and stained with the respective antibodies and DAPI. A spinning disk Perkin Elmer Opera platform equipped with a 20 x water immersion objective (0.7 numerical aperture, Olympus) was employed to acquire 6-10 confocal images (fields) for each well in a single optimised focal plane comprising two fluorescence channels, DAPI or Alexa Fluor 405 and Alexa Fluor 488. The micrographs were analysed using an optimised spot detection script operated by an integrated software package (Acapella, Perkin Elmer). DAPI or Alexa Fluor 405 was used to segment nuclei and create a nuclear mask. Automated mask transferal to the second fluorescence channel (γH2AX, 53BP1 or FK2) allowed detection of intensities and IRIF specifically within the nuclear areas of the detected cells. Key steps of the analysis pipeline are illustrated in Supplementary Fig. 1a. For the IRIF screen (module 1) we imaged

>1 million cells resulting in, on average, >700 cells per condition based on one screening experiment. For a comprehensive overview of the screening data, see Supplementary Figures 1b-c and *PubChem BioAssays*. For the IRIF data regarding siALL-Ds, siRNF138 and siCtIP-treated cells in Figures 6d-e and Supplementary Figures 8a-b, we imaged >8,000 cells per siRNA per staining for Figure 6e and >10,000 cells per siRNA per staining for Supplementary Figure 8a.

IncuCyte cell proliferation/growth rate assays

48 hours after siRNA transfection 30,000 U2OS cells were plated into 24 well dishes and irradiated with the indicated doses of IR the following day. Phase contrast images were acquired every 6 hours over a time period of 168 hours using an IncuCyte microscopy platform (Essen BioScience). Cell confluency percentages were calculated using the integrated Cell Player software and results analysed with Excel (Microsoft Office) for exponential growth periods (confluency percentages <80% and incremental increase >2%). Values represent average increases in confluency for each measured 6-hour increment of the indicated condition normalised to the corresponding undamaged control situation.

Microscopy

Unless stated otherwise fluorescence images of live and fixed cells were acquired using the same microscope, objective and software as described for laser micro-irradiation experiments outlined in the 'DNA damage induction' section. Unless stated otherwise, all microscopy experiments were performed at least twice.

Clonogenic survival assays

U2OS cells were treated with siRNA oligonucleotides and irradiated with IR at the indicated doses. Colony formation occurred over the next 10–14 days under standard cell culture conditions. Colonies were counted after staining with 0.5% crystal violet/20% ethanol. The results were normalised to plating efficiencies.

Quantitative Real-Time PCR (qRT-PCR)

Total RNA of U2OS cells treated with the indicated siRNA oligonucleotides was extracted and purified using the RNeasy Mini Kit (Qiagen) and the TURBO DNA-*free* Kit (Invitrogen) according to the manufacturer's instructions. Superscript III Reverse Transcriptase (Invitrogen) and oligo-d(T) primers contained within the kit were used to prepare cDNA following the manufacturer's guidelines. qRT-PCR experiments were carried out using Fast SYBR Green PCR mastermix (Invitrogen) on a StepOnePlus Real-Time PCR System (Applied Biosystems). Amounts of target mRNA were normalised to an endogenous housekeeping gene (GAPDH) and calculated using the formula: $2^{-\Delta\Delta CT}$. Primer sequences are listed in Supplementary Table 3.

Whole cell extracts and immunoblotting

For siRNA validation, 6 cm dishes of U2OS cells were washed once with PBS, harvested in 100-150 μl 2× Laemmli buffer (120 mM Tris-HCl pH 6.8, 4% SDS and 20% glycerol), incubated for 5 minutes at 95°C, briefly spun and sonicated. Protein concentrations were

determined using a NanoDrop spectrophotometer (Thermo Scientific) at 280 nm followed by addition of bromophenol blue and 2-mercaptoethanol. For all DDR signalling experiments, immunoblotting conditions were as described above but the lysis buffer used contained 50 mM Tris-HCl pH 7.5, 2% SDS, serine/threonine phosphatase inhibitor cocktail (Sigma-Aldrich), protease inhibitor cocktail (Roche) and 10 mM N-ethylmaleimide (Sigma-Aldrich). After 5 minutes at 95°C, SDS–PAGE was performed to resolve proteins on 4-20% Tris/glycine, precast NuPAGE Novex 4-12% Bis/Tris gradient gels (Invitrogen) or precast NuPAGE Novex 3-8% Tris/Acetate gradient gels (Invitrogen). Specifically, experiments shown in Figures 7c-e, 8c and Supplementary Figures 2a-b, 7c, 8d-e were resolved on 4-20% Tris/glycine gels, while in Figures 7f-h and 8b 4-12% Tris/glycine gels were used. In Figure 6c and in Supplementary Figures 3, 4a, 4c, 4e, 7d, 8c and 8f, 4-12% Bis/Tris gels were used and in Supplementary Figure 8g, a 3-8% Tris/acetate gel was used. Separated proteins were transferred to nitrocellulose or PVDF membranes (GE Healthcare) and immunoblotted with the indicated antibodies (Supplementary Table 4). Unless stated otherwise experiments were performed at least twice.

Immunoprecipitation

Cell extracts were prepared by scraping cells from PBS-washed plates into ice-cold lysis buffer (LB, 20 mM Tris-HCl pH 7.5, 40 mM NaCl, 2 mM $MgCl_2$, 10% glycerol and 0.5% NP-40) containing freshly added N-ethylmaleimide (NEM, 10 mM, Sigma-Aldrich), EDTA-free protease inhibitor cocktail (PI, 1×, Roche), EDTA-free serine/threonine phosphatase inhibitor cocktail (PPI, Sigma-Aldrich) and benzonase (10 μl/ml lysis buffer, Novagen 70664-3). After increasing the salt concentration to ~500 mM NaCl, extracts were rotated for 10-15 minutes at room temperature, subsequently diluted 1:2 with lysis buffer (without benzonase supplemented with 6 mM 1,10-Phenanthroline, Sigma-Aldrich) and the extracts cleared by centrifugation at 16,000 g for 0.5-1 hour at 4°C. Immunoprecipitation reactions were rotated for 2 hours to overnight at 4°C using GFP-Trap-A beads (ChromoTek, 10 μl per mg protein) followed by five washes with immunoprecipitation buffer (lysis buffer without benzonase containing a final concentration of ~250 mM NaCl). Proteins were eluted from the GFP-Trap-A beads in a 5-10-minute incubation step at 95°C in 1.5× SDS sample buffer and immunoblotted as described in the respective section. For immunoprecipitation experiments shown in Figure 7e and Supplementary Figure 8e the procedure is as described above but the NaCl concentration (500 mM) was kept throughout including all 5 subsequent washes. Unless stated otherwise experiment were performed at least twice.

Immunofluorescence

Cells were washed with PBS containing 0.1% Tween-20 (PBST) and – for FK2, RPA2 and BrdU staining – pre-extracted for 10-15 minutes with buffer containing 25 mM HEPES pH 7.4, 50 mM NaCl, 1 mM EDTA, 3 mM $MgCl_2$, 300 mM sucrose and 0.5% Triton X-100 followed by a 20-minute fixation step in PBS containing 2% formaldehyde (w/v). For all other immunofluorescence experiments pre-extraction was omitted and cells were permeabilised for 10-15 minutes with 0.2-0.5% Triton X-100 in PBS after fixation. After three washes with PBST immunostaining was conducted with the indicated primary antibodies (Supplementary Table 4) diluted in blocking buffer (5% BSA in PBST) for 1 hour at room temperature or overnight at 4°C. After three PBST washing steps, cells were stained

with the appropriate secondary antibodies (Supplementary Table 4) diluted in blocking buffer (1 hour at room temperature) followed by three washes with PBST. Unless stated otherwise cells were counterstained with DAPI (2-5 μg/ml) and mounted using Vectashield (Vector labs).

Statistics and analyses

Unless stated otherwise Prism 6 (GraphPad Software) was used to calculate p-values based on Mann Whitney analyses. Data were considered statistically significant for p-values <0.05. Unless otherwise specified, statistical analyses are based on at least three biologically independent experiments. The CLC Main Workbench software package was used for protein alignments and the open source software package R for bubble plots (Fig. 3b, and Supplementary Fig. 2d). Unless stated otherwise, microscopy image analyses were performed using the open software packages ImageJ and FIJI or FV-10 software (Olympus). Specifically, nuclei were manually segmented using the DAPI channel and the resulting regions of interest transferred to the fluorescence channel of interest (RPA2, BrdU or CtIP). For intensity quantifications of CtIP laser lines, average CtIP intensities along laser tracks were measured and ratios of CtIP average line intensities over average nucleoplasm intensities were calculated and compared. Unless stated otherwise, Excel (Microsoft Office), Prism 6 (GraphPad Software) or CLC Main Workbench were used for data visualisation.

Reproducibility of experiments

Excluding screening experiments that have been performed once, all other experiments were performed at least twice unless specified otherwise. Note that the increase in ubiquitylation in siALL-Ds- over siCTRL-treated cells in Figure 7g in the absence of DNA damage is due to experimental variation rather than biological significance.

Circos plot

Circular visualisation[51] was used to illustrate complex DDR fingerprints of siE2 pools contained in key readouts of all three screening modules. Effects were normalised to siCTRL treatments for each readout. Increases in readouts were set to 0.

Cell-cycle profiling

U2OS cells were treated with siRNA and fixed with 70% ethanol. After RNAse A (250 μg/ml) and propidium iodide (10 μg/ml) incubation for 30 minutes at 37°C cells were analysed by flow-cytometry on a FACSCalibur flow-cytometer (BD Biosciences) using the CellQuest software. Results were analysed using FlowJo (TreeStar) to calculate the percentage of cells in different cell-cycle phases using two algorithms, Watson Pragmatic (WP) and Dean-Jett-Fox (DJF).

DNA pull-down experiments

Magnetic streptavidin dynabeads (Dynal, M-280; 50 μl bead-slurry per reaction) were washed twice with $2 \times$ Binding and Washing buffer ($2 \times$ B&W buffer; 10 mM Tris-HCl pH 7.4 and 2 M NaCl) and subsequently rotated for 15 minutes at room temperature in the presence of 5 pmol of 5′-biotinylated or untagged DNA oligonucleotides of the sequence 5′-

ATCGCATTGGCATTGGCAATGCGATACGACTGATCGAGGGTACTCAGCTAGCTGAT TCCGATCGGCTTATTCCGTGTACATACATCGGAT-3′. After washing three times with 1x B&W and twice with blocking buffer (50 mM Hepes, 150 mM NaCl, 0.05 mg/mL BSA and 0.02% NP-40), the beads were rotated for 30 minutes at room temperature in the presence of blocking buffer. Upon removal of the blocking buffer, the beads were rotated for 45 minutes at room temperature in 500 μl blocking buffer containing 600 ng of bacteria-purified His-SUMO-RNF138-WT or -ZNFs, followed by four washes with blocking buffer. His-SUMO-RNF138-WT or -ZNFs were eluted from the beads in a 10-minute incubation step at 95°C in 1.5× SDS sample buffer and immunoblotted as described in the respective section.

Bacterial protein expression and purification

His-SUMO-RNF138 and UBE2T were expressed and purified based on the protocols of Hodson et al. with minor variations[55]. Briefly, proteins were expressed in Rosetta cells (Novagen) following an overnight IPTG induction at 16 °C, the bacteria lysed in buffer containing 0.5 M NaCl, 100 mM Tris pH 8.0, 250 μM TCEP and protease inhibitors (Roche) and the clarified lysates incubated with Ni-NTA (Qiagen). Proteins were eluted with 300 mM imidazole and dialysed to remove the imidazole. RNF138 retained the His-SUMO tag, whereas the His tag was removed from UBE2T using PreScission Protease (GE Healthcare) overnight at 4 °C.

In vitro ubiquitylation assays

In vitro ubiquitylation assays were performed in 20 μL reactions in the presence of 50 mM HEPES-NaOH pH 8.0, 100 mM NaCl, 3 mM ATP/Mg (Sigma Aldrich, A9187), 0.1 μM UBE1 (Boston Biochem, E-304), 30 μM biotin-Ub (Boston Biochem, UB-560), 3 μM UBE2D1 (Boston Biochem, E2-616) or 0.5 μM UBE2T and 0.2 μM His-SUMO RNF138. Reactions were incubated at 37 °C for 30-60 minutes and overnight at room temperature in the presence of 0.5 mM DTT for CtIP. The reactions were terminated by the addition of SDS-PAGE sample buffer containing reducing agent and subsequent boiling at 95 °C for 3 minutes. Samples were subjected to SDS-PAGE and analysed by immunoblotting.

LC-MS/MS to map ubiquitylated lysines on CtIP

HEK293 cells transiently expressing GFP-CtIP were irradiated (IR, 15 Gy) and after 20 minutes recovery cell were harvested, lysed and GFP-CtIP was immunoprecipitated according to the 'Immunoprecipitation' paragraph above, with the exception that washing was done five times with high salt lysis buffer (LB + NEM + PI + PPI, 1 M NaCl) and twice with low salt lysis buffer (LB + NEM + PI + PPI) in the end. Immunoprecipitated GFP-CtIP was resolved by SDS-PAGE and in-gel-digested using trypsin. A quadrupole Orbitrap mass spectrometer (Q-Exactive Plus, Thermo Scientific) equipped with an EASY-nLC II nanoflow HPLC system (Thermo Scientific) was used to analyse the peptide fractions[56]. Analyses of raw data were performed using MaxQuant (development version 1.3.9.21)[57]. Andromeda search engine[58] was used to search parent ion and MS2 spectra against 88,473 human protein sequences retrieved from the December 2013 UniProt knowledge base. Spectra were searched with a mass tolerance of 6 ppm in MS mode, 20 ppm in HCD MS2 mode, strict trypsin specificity and allowing up to two missed cleavage sites. Cysteine

carbamidomethylation was included as a fixed modification and N-terminal protein acetylation, methionine oxidation, n-ethylmaleimide modification of cysteines, diglycine-lysine were included as variable modifications.. The probabilities of site localisations were determined using MaxQuant based on the PTM scoring algorithm57. Filtering of the dataset was based on posterior error probability (PEP) to arrive at a false discovery rate of 1% for peptide spectrum matches and protein groups. The 14 lysines in CtIP were identified based on two biological replicates and occurred in either one or both of the experiments.

Plasmids and cloning

Plasmids used in the TLR assays have been described previously14. pEGFP-C1 (Clontech) vectors containing UBE2D1 (WT and C85S), UBE2D2, UBE2D3, UBE2D4, UBE2K, UBE2L3, UBE2L6, and UBE2R1 with 5' XhoI and 3' HindIII as cloning sites, UBE2J1 with 5' XhoI and 3' BamHI as cloning sites and UBE2J2, UBE2O and UBE2R2 with 5' HindIII and 3' EcoRI as cloning sites were purchased from Genewiz. Plasmids for tet-on inducible expression of siALL-Ds resistant UBE2D1 (WT and C85S) in mammalian cells were generated according to the following: firstly, UBE2D1 (WT and C85S) cassettes were sub-cloned from pEGFP-C1 into a tetracycline operator (TO)-containing pEGFP-C1 (pEGFP-C1/TO) using XhoI and HindIII. Secondly, we inserted six silent mutations into the siUBE2D1-2 target sequence in UBE2D1 C85S and an additional five silent mutations into the partial siUBE2D2-1 target sequence in UBE2D1 WT using the QuikChange Lightning Site-Directed Mutagenesis Kit (Agilent Technologies) according to the manufacturer's instructions with pEGFP-C1/TO-UBE2D1 (WT and C85S) as templates and siUBE2D1-2res-D1_f and siUBE2D1-2res-D1_r (WT and C85S) or siUBE2D2-1res-D1_f and siUBE2D2-1res-D1_r (WT) as primers (Supplementary Table 3). pEGFP-C1 vectors containing RNF138 (WT, UIM, ZNF (86-215)) with 5' XhoI and 3' BamHI as cloning sites were purchased from Genewiz. pEGFP-C1 containing the RNF138 C18/21A double mutant was generated using the QuikChange Lightning Site-Directed Mutagenesis Kit (Agilent Technologies) according to the manufacturer's instructions with pEGFP-C1-RNF138 WT as a template and 138-C18/21A_f and 138-C18/21A_r as primers (Supplementary Table 3). Mammalian expression plasmids for RFP- and HA-RNF138 WT were generated by sub-cloning RNF138 WT from pEGFP-C1 into pmRFP-C1 (pEGFP-C1 containing monomeric RFP (mRFP) instead of GFP) and HA-pcDNA3.1(-) (HA tag inserted into pcDNA3.1(-) (Life Technologies) between NheI and XhoI sites) using XhoI and BamHI. Mammalian expression plasmids for tet-on inducible expression of siRNF138-1-resistant GFP-RNF138 (WT and C18/21A) were obtained according to the following: firstly, we PCR-amplified the GFP-RNF138 (WT and C18/21A) cassettes contained within pEGFP-C1 using primers HindIII-GFP_f and 138-BamHI_r (Supplementary Table 3) and inserted the digested products into the HindIII and BamHI sites of pcDNA4/TO (Invitrogen). Secondly, we induced six silent mutations contained within the target sequence of siRNF138-1 into RNF138 (WT and C18/21A) using the QuikChange Lightning Site-Directed Mutagenesis Kit (Agilent Technologies) according to the manufacturer's instructions with pcDNA4/TO-GFP-RNF138 (WT and C18/21A) as templates and si138-1res138_f and si138-1res138_r as primers (Supplementary Table 3). pcDNA4/TO-GFP was a gift from Yossi Shiloh. Bacterial expression plasmids for His-SUMO-RNF138, wildtype and ZNFs, were obtained according to the following: firstly, we PCR-amplified

the RNF138 cassette contained within the corresponding pEGFP-C1-RNF138 plasmid using primers His-SUMO_NcoI_f and His-SUMO_XhoI_r (Supplementary Table 3) and inserted the digested products into the NcoI and XhoI sites of the pET-backbone vector pCri-11a (Addgene #61319). The GFP-CtIP plasmid (pEGFP-C1 containing siCtIP resistant WT CtIP) was described previously4. We performed QuikChange Lightning Multi Site-Directed Mutagenesis (Agilent Technologies) according to the manufacturer's instructions to generate GFP-CtIP-12KR, -6KR and -5KR plasmids using GFP-CtIP plasmid as a template together with CtIP mutagenesis primers (Supplementary Table 3). A mammalian expression plasmid encoding 3x HA-Ubiquitin was previously generated together with the laboratories of Yossi Shiloh and Moshe Oren. The bacterial expression plasmid for UBE2T was provided by the Philip Cohen laboratory (DU12416; pET156P UBE2T). DNA constructs were validated by sequencing. Primers were acquired from Sigma-Aldrich.

PubChem BioAssays deposition

The original screening data are available at http://www.ncbi.nlm.nih.gov/pcassay under AID accession numbers 1159544 (results for γH2AX, 53BP1 and FK2 foci kinetics after IR), 1159543 & 1159541 (TLR; HR results for siRNAs and small molecule inhibitors, respectively), 1159542 & 1159539 (TLR; mutEJ results for siRNAs and small molecule inhibitors, respectively), 1159546 &1159547 (results for pCHK1 after camptothecin for siRNAs and small molecule inhibitors, respectively), 1159538 & 1159540 (results for pCHK1 after IR for siRNAs and small molecule inhibitors, respectively), 1159545 & 1159548 (results for pRPA2 after camptothecin for siRNAs and small molecule inhibitors, respectively) and 1159549 (summary).

Supplementary Material

Refer to Web version on PubMed Central for supplementary material.

Acknowledgements

References

1. Jackson SP, Bartek J. The DNA-damage response in human biology and disease. Nature. 2009; 461:1071–8. [PubMed: 19847258]

2. Ciccia A, Elledge SJ. The DNA damage response: making it safe to play with knives. Mol Cell. 2010; 40:179–204. [PubMed: 20965415]

3. Deriano L, Roth DB. Modernizing the nonhomologous end-joining repertoire: alternative and classical NHEJ share the stage. Annu Rev Genet. 2013; 47:433–55. [PubMed: 24050180]

4. Sartori AA, et al. Human CtIP promotes DNA end resection. Nature. 2007; 450:509–14. [PubMed: 17965729]

5. Greenberg RA, et al. Multifactorial contributions to an acute DNA damage response by BRCA1/ BARD1-containing complexes. Genes Dev. 2006; 20:34–46. [PubMed: 16391231]

6. Shiloh Y, Ziv Y. The ATM protein kinase: regulating the cellular response to genotoxic stress, and more. Nat Rev Mol Cell Biol. 2013; 14:197–210.

7. Polo SE, Jackson SP. Dynamics of DNA damage response proteins at DNA breaks: a focus on protein modifications. Genes Dev. 2011; 25:409–33. [PubMed: 21363960]

8. Jackson SP, Durocher D. Regulation of DNA damage responses by ubiquitin and SUMO. Mol Cell. 2013; 49:795–807. [PubMed: 23416108]

9. Kulathu Y, Komander D. Atypical ubiquitylation - the unexplored world of polyubiquitin beyond Lys48 and Lys63 linkages. Nat Rev Mol Cell Biol. 2012; 13:508–23. [PubMed: 22820888]

10. Husnjak K, Dikic I. Ubiquitin-binding proteins: decoders of ubiquitin-mediated cellular functions. Annu Rev Biochem. 2012; 81:291–322. [PubMed: 22482907]

11. Wenzel DM, Stoll KE, Klevit RE. E2s: structurally economical and functionally replete. Biochem J. 2011; 433:31–42. [PubMed: 21158740]

12. Ye Y, Rape M. Building ubiquitin chains: E2 enzymes at work. Nat Rev Mol Cell Biol. 2009; 10:755–64. [PubMed: 19851334]

13. Povlsen LK, et al. Systems-wide analysis of ubiquitylation dynamics reveals a key role for PAF15 ubiquitylation in DNA-damage bypass. Nat Cell Biol. 2012; 14:1089–98. [PubMed: 23000965]

14. Certo MT, et al. Tracking genome engineering outcome at individual DNA breakpoints. Nat Methods. 2011; 8:671–6. [PubMed: 21743461]

15. Davies OR, et al. CtIP tetramer assembly is required for DNA-end resection and repair. Nat Struct Mol Biol. 2015; 22:150–157. [PubMed: 25558984]

16. Jazayeri A, et al. ATM- and cell cycle-dependent regulation of ATR in response to DNA double-strand breaks. Nat Cell Biol. 2006; 8:37–45. [PubMed: 16327781]

17. Murakawa Y, et al. Inhibitors of the proteasome suppress homologous DNA recombination in mammalian cells. Cancer Res. 2007; 67:8536–43. [PubMed: 17875693]

18. Zhou Y, Caron P, Legube G, Paull TT. Quantitation of DNA double-strand break resection intermediates in human cells. Nucleic Acids Res. 2014; 42:e19. [PubMed: 24362840]

19. Polato F, et al. CtIP-mediated resection is essential for viability and can operate independently of BRCA1. J Exp Med. 2014; 211:1027–36. [PubMed: 24842372]

20. Kakarougkas A, et al. Co-operation of BRCA1 and POH1 relieves the barriers posed by 53BP1 and RAP80 to resection. Nucleic Acids Res. 2013; 41:10298–311. [PubMed: 24013561]

21. Long DT, Joukov V, Budzowska M, Walter JC. BRCA1 Promotes Unloading of the CMG Helicase from a Stalled DNA Replication Fork. Mol Cell. 2014; :1–12. DOI: 10.1016/j.molcel.2014.08.012

22. Cruz-García A, López-Saavedra A, Huertas P. BRCA1 Accelerates CtIP-Mediated DNA-End Resection. Cell Rep. 2014; :451–459. DOI: 10.1016/j.celrep.2014.08.076 [PubMed: 25310973]

23. Machida YJ, et al. UBE2T is the E2 in the Fanconi anemia pathway and undergoes negative autoregulation. Mol Cell. 2006; 23:589–96. [PubMed: 16916645]

24. Zhang Y, et al. UBE2W interacts with FANCL and regulates the monoubiquitination of Fanconi anemia protein FANCD2. Mol Cells. 2011; 31:113–22. [PubMed: 21229326]

25. Maréchal A, et al. PRP19 transforms into a sensor of RPA-ssDNA after DNA damage and drives ATR activation via a ubiquitin-mediated circuitry. Mol Cell. 2014; 53:235–46. [PubMed: 24332808]

26. Adamson B, Smogorzewska A, Sigoillot FD, King RW, Elledge SJ. A genome-wide homologous recombination screen identifies the RNA-binding protein RBMX as a component of the DNA-damage response. Nat Cell Biol. 2012; 14:318–28. [PubMed: 22344029]

27. Ikura T, et al. DNA damage-dependent acetylation and ubiquitination of H2AX enhances chromatin dynamics. Mol Cell Biol. 2007; 27:7028–40. [PubMed: 17709392]

28. Liu C, et al. RNF168 forms a functional complex with RAD6 during the DNA damage response. J Cell Sci. 2013; 126:2042–51. [PubMed: 23525009]

29. Jacquemont C, Taniguchi T. Proteasome function is required for DNA damage response and fanconi anemia pathway activation. Cancer Res. 2007; 67:7395–405. [PubMed: 17671210]

30. Matsuoka S, et al. ATM and ATR substrate analysis reveals extensive protein networks responsive to DNA damage. Science. 2007; 316:1160–6. [PubMed: 17525332]

31. Gudjonsson T, et al. TRIP12 and UBR5 suppress spreading of chromatin ubiquitylation at damaged chromosomes. Cell. 2012; 150:697–709. [PubMed: 22884692]

32. Parsons JL, et al. CHIP-mediated degradation and DNA damage-dependent stabilization regulate base excision repair proteins. Mol Cell. 2008; 29:477–87. [PubMed: 18313385]

33. Inagaki A, et al. Human RAD18 interacts with ubiquitylated chromatin components and facilitates RAD9 recruitment to DNA double strand breaks. PLoS One. 2011; 6:e23155. [PubMed: 21858012]

34. Watanabe K, et al. RAD18 promotes DNA double-strand break repair during G1 phase through chromatin retention of 53BP1. Nucleic Acids Res. 2009; 37:2176–93. [PubMed: 19228710]

35. Giannini AL, Gao Y, Bijlmakers M-J. T-cell regulator RNF125/TRAC-1 belongs to a novel family of ubiquitin ligases with zinc fingers and a ubiquitin-binding domain. Biochem J. 2008; 410:101–11. [PubMed: 17990982]

36. Yamada M, et al. NARF, an nemo-like kinase (NLK)-associated ring finger protein regulates the ubiquitylation and degradation of T cell factor/lymphoid enhancer factor (TCF/LEF). J Biol Chem. 2006; 281:20749–60. [PubMed: 16714285]

37. Polanowska J, Martin JS, Garcia-Muse T, Petalcorin MIR, Boulton SJ. A conserved pathway to activate BRCA1-dependent ubiquitylation at DNA damage sites. EMBO J. 2006; 25:2178–88. [PubMed: 16628214]

38. You Z, et al. CtIP links DNA double-strand break sensing to resection. Mol Cell. 2009; 36:954–69. [PubMed: 20064462]

39. Morris JR, Solomon E. BRCA1 : BARD1 induces the formation of conjugated ubiquitin structures, dependent on K6 of ubiquitin, in cells during DNA replication and repair. Hum Mol Genet. 2004; 13:807–17. [PubMed: 14976165]

40. Kaidi A, Weinert BT, Choudhary C, Jackson SP. Human SIRT6 promotes DNA end resection through CtIP deacetylation. Science. 2010; 329:1348–53. [PubMed: 20829486]

41. Andres SN, et al. Tetrameric Ctp1 coordinates DNA binding and DNA bridging in DNA double-strand-break repair. Nat Struct Mol Biol. 2015; 22:158–166. [PubMed: 25580577]

42. Murina O, et al. FANCD2 and CtIP cooperate to repair DNA interstrand crosslinks. Cell Rep. 2014; 7:1030–8. [PubMed: 24794434]

43. Ismail IH, et al. RNF138 is an E3 ubiquitin ligase that displaces Ku to promote DNA end resection and regulate DNA repair pathway choice. Nat Cell Biol.

44. Galanty Y, Belotserkovskaya R, Coates J, Jackson SP. RNF4, a SUMO-targeted ubiquitin E3 ligase, promotes DNA double-strand break repair. Genes Dev. 2012; 26:1179–95. [PubMed: 22661229]

45. Smeenk G, et al. Poly(ADP-ribosyl)ation links the chromatin remodeler SMARCA5/SNF2H to RNF168-dependent DNA damage signaling. J Cell Sci. 2013; 126:889–903. [PubMed: 23264744]

46. Markson G, et al. Analysis of the human E2 ubiquitin conjugating enzyme protein interaction network. Genome Res. 2009; 19:1905–11. [PubMed: 19549727]

47. Gao J, et al. Integrative analysis of complex cancer genomics and clinical profiles using the cBioPortal. Sci Signal. 2013; 6:pl1. [PubMed: 23550210]

48. Paulsen RD, et al. A genome-wide siRNA screen reveals diverse cellular processes and pathways that mediate genome stability. Mol Cell. 2009; 35:228–39. [PubMed: 19647519]

49. Curtin NJ. DNA repair dysregulation from cancer driver to therapeutic target. Nat Rev Cancer. 2012; 12:801–17. [PubMed: 23175119]

50. Mattern MR, Wu J, Nicholson B. Ubiquitin-based anticancer therapy: carpet bombing with proteasome inhibitors vs surgical strikes with E1, E2, E3, or DUB inhibitors. Biochim Biophys Acta. 2012; 1823:2014–21. [PubMed: 22610084]

51. Krzywinski M, et al. Circos: an information aesthetic for comparative genomics. Genome Res. 2009; 19:1639–45. [PubMed: 19541911]

52. You Z, Bailis JM. DNA damage and decisions: CtIP coordinates DNA repair and cell cycle checkpoints. Trends Cell Biol. 2010; 20:402–9. [PubMed: 20444606]

53. Limoli CL, Ward JF. A new method for introducing double-strand breaks into cellular DNA. Radiat Res. 1993; 134:160–9. [PubMed: 7683818]

54. Lukas C, Falck J, Bartkova J, Bartek J, Lukas J. Distinct spatiotemporal dynamics of mammalian checkpoint regulators induced by DNA damage. Nat Cell Biol. 2003; 5:255–60. [PubMed: 12598907]

55. Hodson C, Purkiss A, Miles JA, Walden H. Structure of the human FANCL RING-Ube2T complex reveals determinants of cognate E3-E2 selection. Structure. 2014; 22:337–344. [PubMed: 24389026]

56. Michalski A, et al. Mass Spectrometry-based Proteomics Using Q Exactive, a High-performance Benchtop Quadrupole Orbitrap Mass Spectrometer. Mol Cell Proteomics. 2011; 10 M111.011015.

57. Cox J, Mann M. MaxQuant enables high peptide identification rates, individualized p.p.b.-range mass accuracies and proteome-wide protein quantification. Nat Biotechnol. 2008; 26:1367–72. [PubMed: 19029910]

58. Cox J, et al. Andromeda: A peptide search engine integrated into the MaxQuant environment. J Proteome Res. 2011; 10:1794–1805. [PubMed: 21254760]

59. Shibata E, Abbas T, Huang X, Wohlschlegel JA, Dutta A. Selective ubiquitylation of p21 and Cdt1 by UBCH8 and UBE2G ubiquitin-conjugating enzymes via the CRL4Cdt2 ubiquitin ligase complex. Mol Cell Biol. 2011; 31:3136–45. [PubMed: 21628527]

60. Zhong Q, Gao W, Du F, Wang X. Mule/ARF-BP1, a BH3-only E3 ubiquitin ligase, catalyzes the polyubiquitination of Mcl-1 and regulates apoptosis. Cell. 2005; 121:1085–95. [PubMed: 15989957]

61. Doil C, et al. RNF168 binds and amplifies ubiquitin conjugates on damaged chromosomes to allow accumulation of repair proteins. Cell. 2009; 136:435–46. [PubMed: 19203579]

62. Galanty Y, et al. Mammalian SUMO E3-ligases PIAS1 and PIAS4 promote responses to DNA double-strand breaks. Nature. 2009; 462:935–9. [PubMed: 20016603]

63. Biton S, et al. Nuclear ataxia-telangiectasia mutated (ATM) mediates the cellular response to DNA double strand breaks in human neuron-like cells. J Biol Chem. 2006; 281:17482–91. [PubMed: 16627474]

64. Bruun D, et al. siRNA depletion of BRCA1, but not BRCA2, causes increased genome instability in Fanconi anemia cells. DNA Repair (Amst). 2003; 2:1007–1013. [PubMed: 12967657]

65. Chapman JR, et al. RIF1 is essential for 53BP1-dependent nonhomologous end joining and suppression of DNA double-strand break resection. Mol Cell. 2013; 49:858–71. [PubMed: 23333305]

66. Biard DSF. Untangling the relationships between DNA repair pathways by silencing more than 20 DNA repair genes in human stable clones. Nucleic Acids Res. 2007; 35:3535–50. [PubMed: 17483520]

67. Liang L, et al. Human DNA ligases I and III, but not ligase IV, are required for microhomology-mediated end joining of DNA double-strand breaks. Nucleic Acids Res. 2008; 36:3297–310. [PubMed: 18440984]

68. Ito M, et al. Rad51 siRNA delivered by HVJ envelope vector enhances the anti-cancer effect of cisplatin. J Gene Med. 2005; 7:1044–1052. [PubMed: 15756713]

69. Lubas M, et al. Interaction profiling identifies the human nuclear exosome targeting complex. Mol. Cell. 2011; 43:624–37. [PubMed: 21855801]

70. Michelle C, Vourc'h P, Mignon L, Andres CR. What was the set of ubiquitin and ubiquitin-like conjugating enzymes in the eukaryote common ancestor? J Mol Evol. 2009; 68:616–28. [PubMed: 19452197]
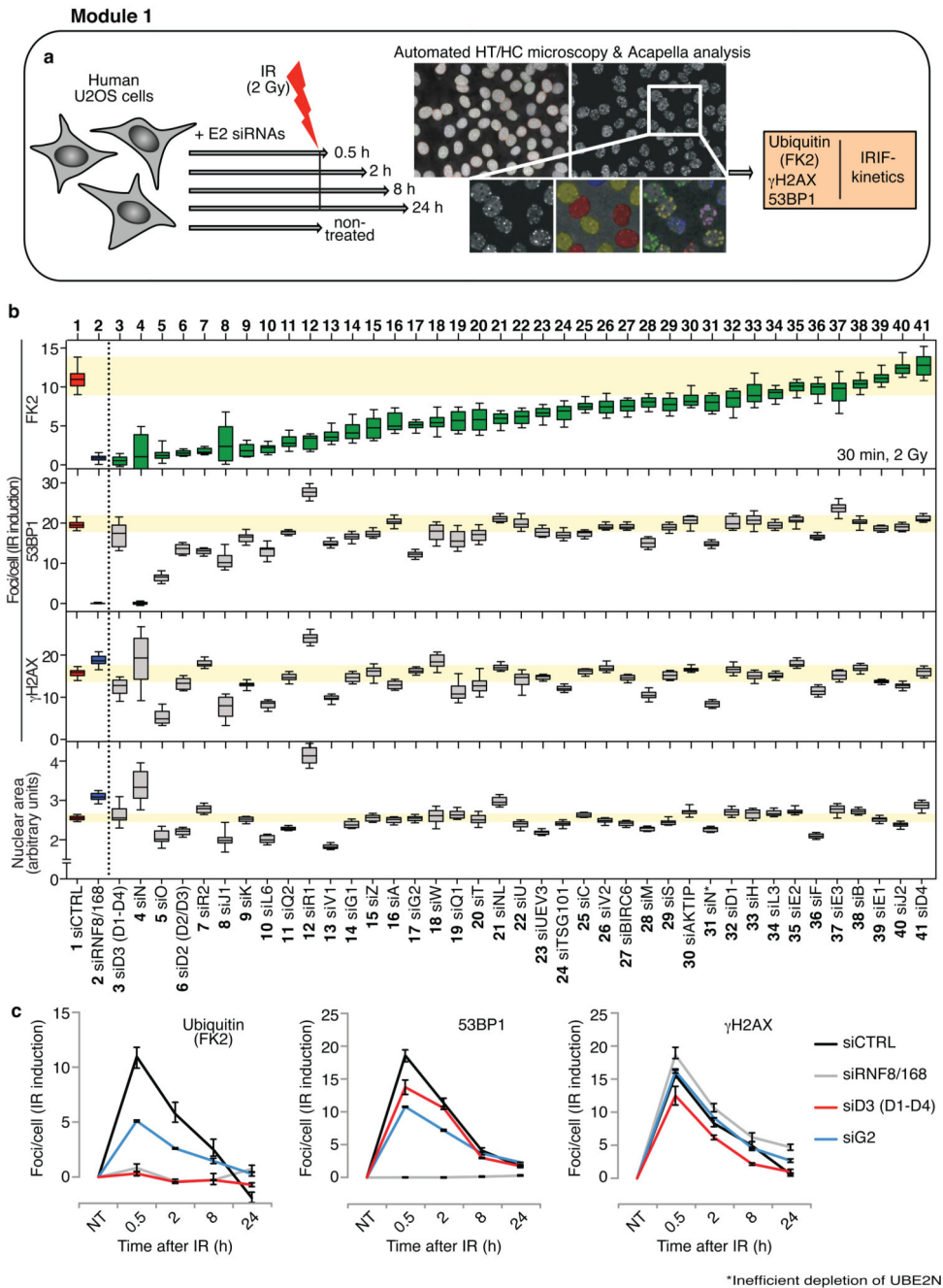
Figure 1. Screening E2s for IRIF-kinetics.
a, Experimental pipeline for module 1 encompassing automated 96-plate format high-throughput/high-content quantitative imaging (spinning disk Opera platform) and automated IRIF detection (Acapella spot detection) of γH2AX (a DNA-damage marker), 53BP1 and conjugated ubiquitin (FK2 antibody) in a total of >1 million cells. **b,** IRIF induction per cell and average nuclear area, 30 minutes post-irradiation. Negative control siRNA targeting luciferase (siCTRL) and positive control siRNA mix targeting RNF8 plus RNF168 are marked in red and blue, respectively. Plots represent medians of n=80 (siCTRL and

siRNF8+168) or n=20 (all other siRNAs) 96-plate-well image fields (lines in boxes), 25-75 percentiles (boxes) and 10-90 percentiles (whiskers) of, on average, 704 imaged cells per siRNA based on one screening experiment. **c**, Full IRIF-kinetics of selected siE2s. Data represent averages ± range of n=8 (siCTRL and siRNF8+168) or n=2 (all other siRNAs) 96-microplate-wells of, on average, 704 imaged cells per siRNA based on one screening experiment. Note that siD3-2 co-depletes all UBE2Ds and siD2-1 co-depletes UBE2D2, UBE2D3 and, to a lesser extent, UBE2D1 (Supplementary Fig. 4a). See Supplementary Figure 1c and *PubChem BioAssays* for a comprehensive overview of screening data. siG2=siUBE2G2.
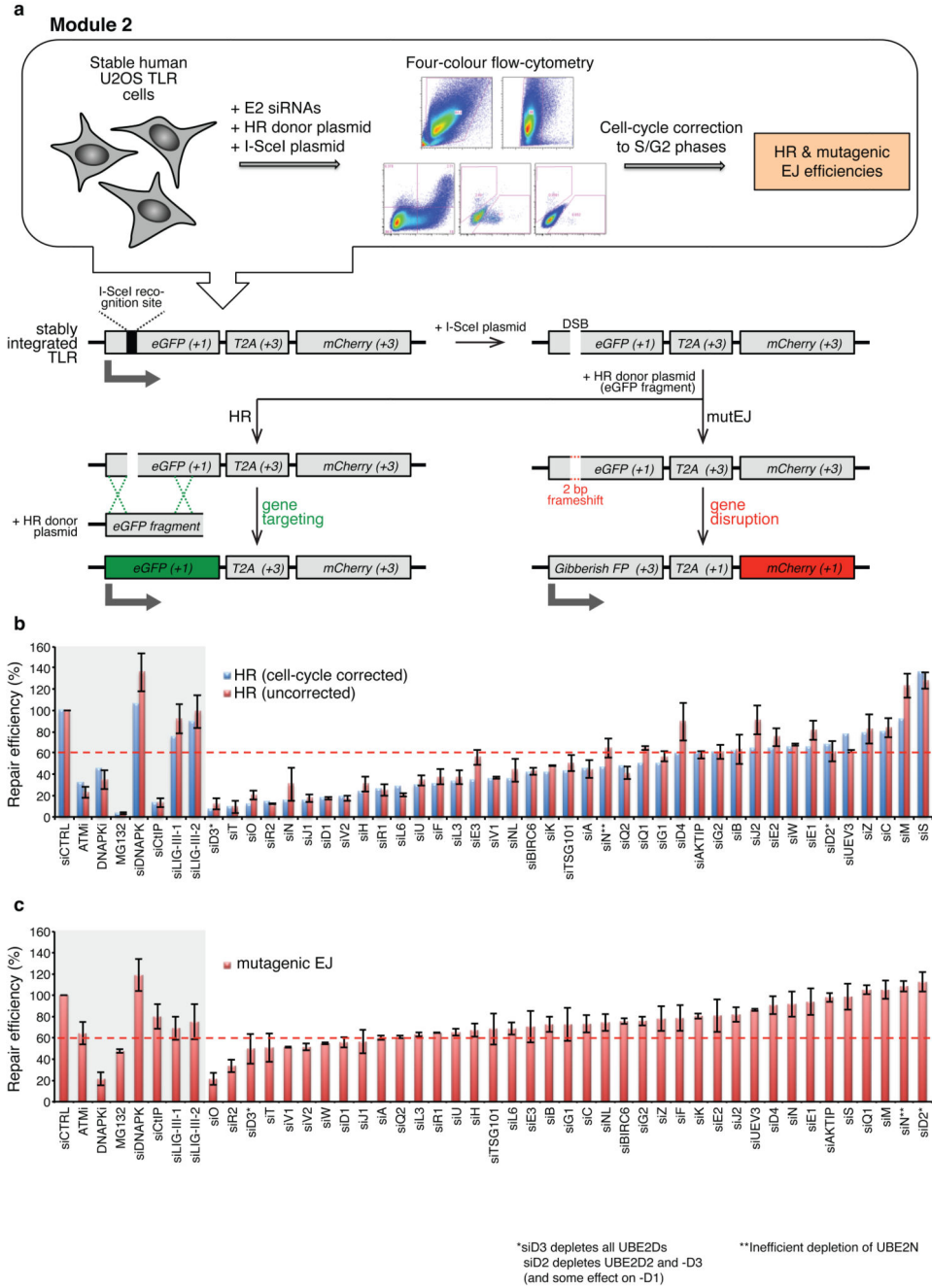
Figure 2. Screening E2s for DSB repair.

a, Schematic of pipeline for module 2 TLR assay14,15 **b,** TLR results for HR. Note that, as HR can only occur in S/G2, data were corrected to flow-cytometry S/G2 values. Grey boxes highlight control siRNA oligonucleotides, dotted line represents arbitrary cut-off at 60%. Data represent means ± SDs for, on average, n=5 biological experiments for controls and a minimum of n=3 for siE2s. See Supplementary Table 2 for precise n values for each condition. **c,** TLR results for mutEJ. Grey boxes highlight control siRNAs, dotted line represents arbitrary cut-off at 60%. Data represent means ± SDs for, on average, n=5

biological experiments for controls and a minimum of n=3 for siE2s. See Supplementary Table 2 for precise n values for each condition. Note: depleting the NHEJ factor DNA-PKcs or MMEJ factor ligase III3 did not affected mutEJ significantly, suggesting that both pathways act redundantly in this assay. Note that siD3-2 co-depletes all UBE2Ds and siD2-1 co-depletes UBE2D2, UBE2D3 and, to a lesser extent, UBE2D1 (Supplementary Fig. 4a). See *PubChem BioAssays* for a comprehensive overview of screening data.
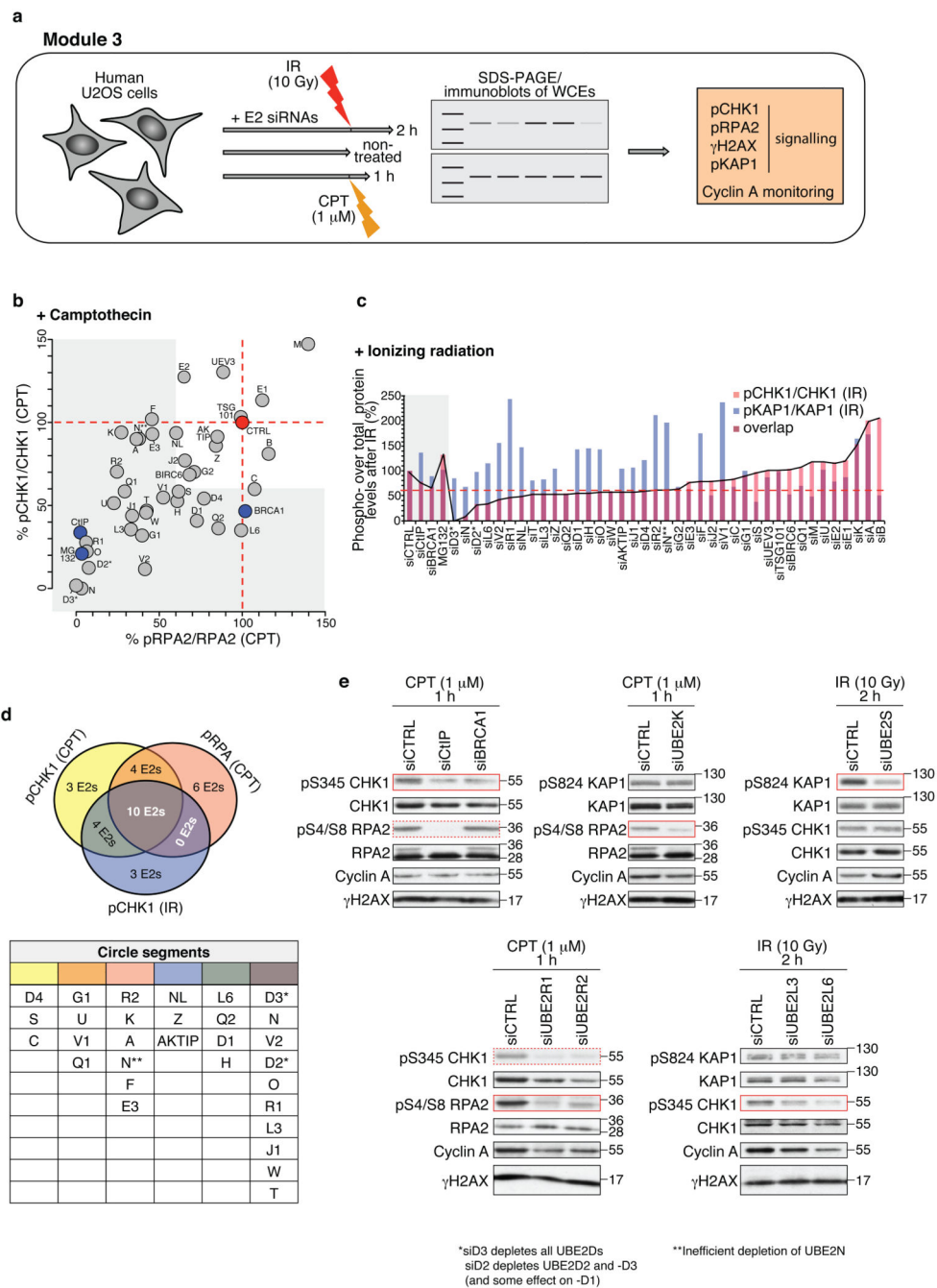
Figure 3. Screening E2s for DDR signalling.
a, Schematic of module 3 encompassing immunoblotting of DDR signalling events after camptothecin or IR-treatment. **b, c,** Quantification of key module 3 readouts following camptothecin (CPT) or IR, respectively, based on immunoblots shown in Supplementary Fig. 2a. Results represent ratios of phosphorylated over total protein levels e.g. phospho-CHK1/total CHK1, which were normalised to the corresponding ratio of siCTRL-treated cells and from which the equivalent ratios in undamaged cells were subtracted. In b, negative control siRNA (siCTRL) and positive controls are highlighted in red and blue, respectively.

Grey background shows regions of >40% reductions. In c, a grey box highlights controls and the dotted red line indicates arbitrary cut-off at 60%. **d,** Overlaps of siE2s scoring with >40% reductions in indicated module 3 readouts. **e,** Whole cell extract (WCE) immunoblot examples for selected siE2 pools based on one screening experiment. Red frames highlight key readouts that the indicated siE2 pools score in, based on their quantification by densitometry as indicated above in b and c. Dotted red frame indicates that only one of the two siE2 pools shows a clear phenotype in the indicated readout. Note: siD3-2 co-depletes all UBE2Ds and siD2-1 codepletes UBE2D2, UBE2D3 and, to a lesser extent, UBE2D1 (Supplementary Fig. 4a). See *PubChem BioAssays* for a comprehensive overview of quantitative screening data.
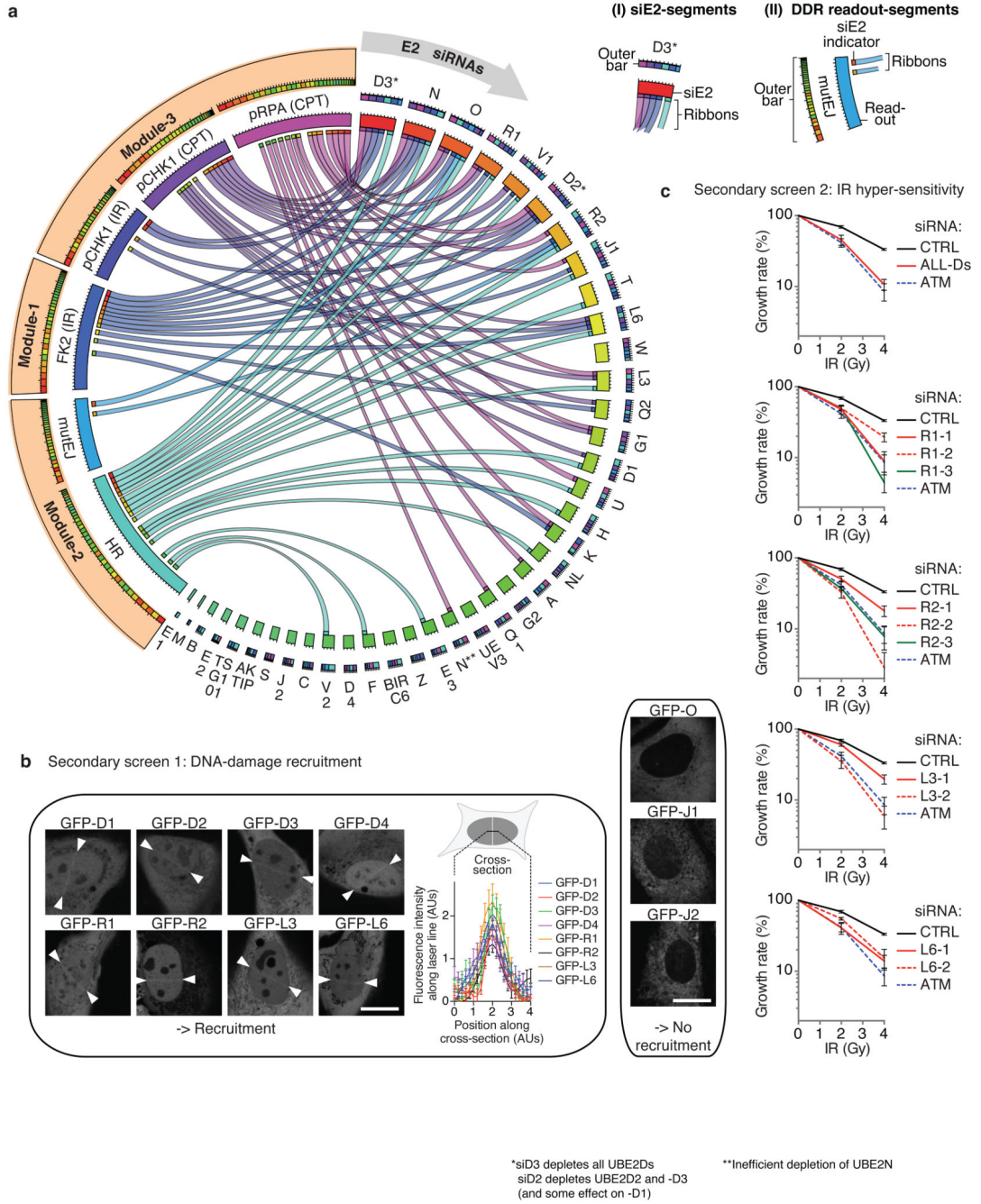
Figure 4. DDR validation of selected E2s.

a, Circos plot51; see legend on top right of the panel: (I) Legend for siE2-segments (arranged clockwise underneath the grey arrow on the right half of the Circos plot according to decreasing overall DDR effects). Outer bar: colour indicates readouts that this siE2 scores in; elements are ordered clockwise for decreasing contributions of individual readouts giving a cumulative impact for each siE2; width of element indicates strength of phenotype. siE2: colour-coded; segment width reflects cumulative impact of all readouts that the respective siE2 scores in; ordered clockwise for siE2s with decreasing cumulative impact. Ribbons:

colours according to read-out, ordered according to readout-segments on the left half of the circle; only for siE2s scoring in top 25 percentile (siE2 values pooled from all modules; siCTRL set to 100%); ribbon width constant for all siE2s. (II) Legend for key DDR readout-segments located underneath orange rim on the left (arranged on left half of Circos plot). Outer bar: colour indicates siE2s scoring in this module readout; ordered clockwise corresponding to decreasing strength of individual siE2 effect; width indicates strength of phenotype. Ribbons: ordered according to siE2 segment list on other half of circle (see also above for siE2s). Read-out: colour-coded, segment width reflects cumulative impact of all siE2s scoring in this module. **b,** Live-cell laser micro-irradiation analyses of transiently expressed GFP-E2s. Data represent fluorescence intensity means of n=9 (UBE2D1), n=6 (UBE2D2), n=3 (UBE2D3), n=3 (UBE2D4), n=6 (UBE2R1), n=9 (UBE2R2), n=12 (UBE2L3) and n=18 (UBE2L6) measurements ± SEM based on three measured sites across each laser tract. **c,** Incucyte cell proliferation/growth rate assays. Data represent medians ± SEM of n=10 experiments for controls and n=8 for siE2s. Statistics source data for this panel can be found in Supplementary Table 5. Scale bar=10 μm. AUs: arbitrary units; see *PubChem BioAssays* for a comprehensive overview of screening data.
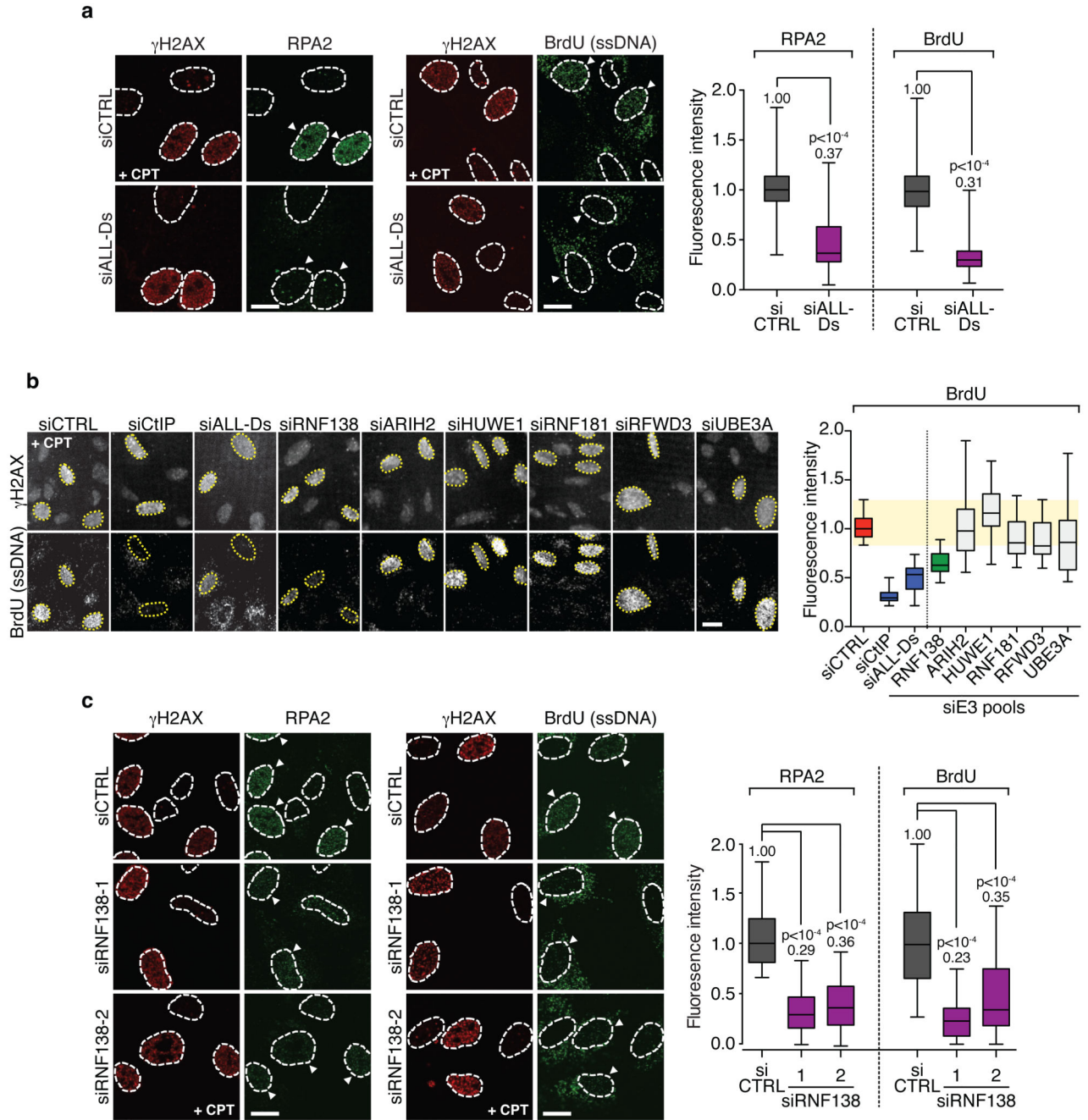
Figure 5. DNA-end resection links UBE2Ds with RNF138.
a, Defects in camptothecin (CPT)-induced RPA2 foci and ssDNA-generation (BrdU) in siALL-Ds treated cells. Dotted outlines represent nuclei according to DAPI staining. Quantifications were performed exclusively in γH2AX-positive nuclei (see arrowheads), representing actively replicating S phase cells that encountered CPT-trapped TopI. Negative control siRNA (siCTRL) is shown in grey. Plots represent RPA2 or BrdU fluorescence intensity medians (lines in boxes; numbers above whiskers), 25-75 percentiles (boxes) and overall ranges (whiskers) of n=161 (siCTRL) and 222 (siALL-Ds) γH2AX-positive cells for
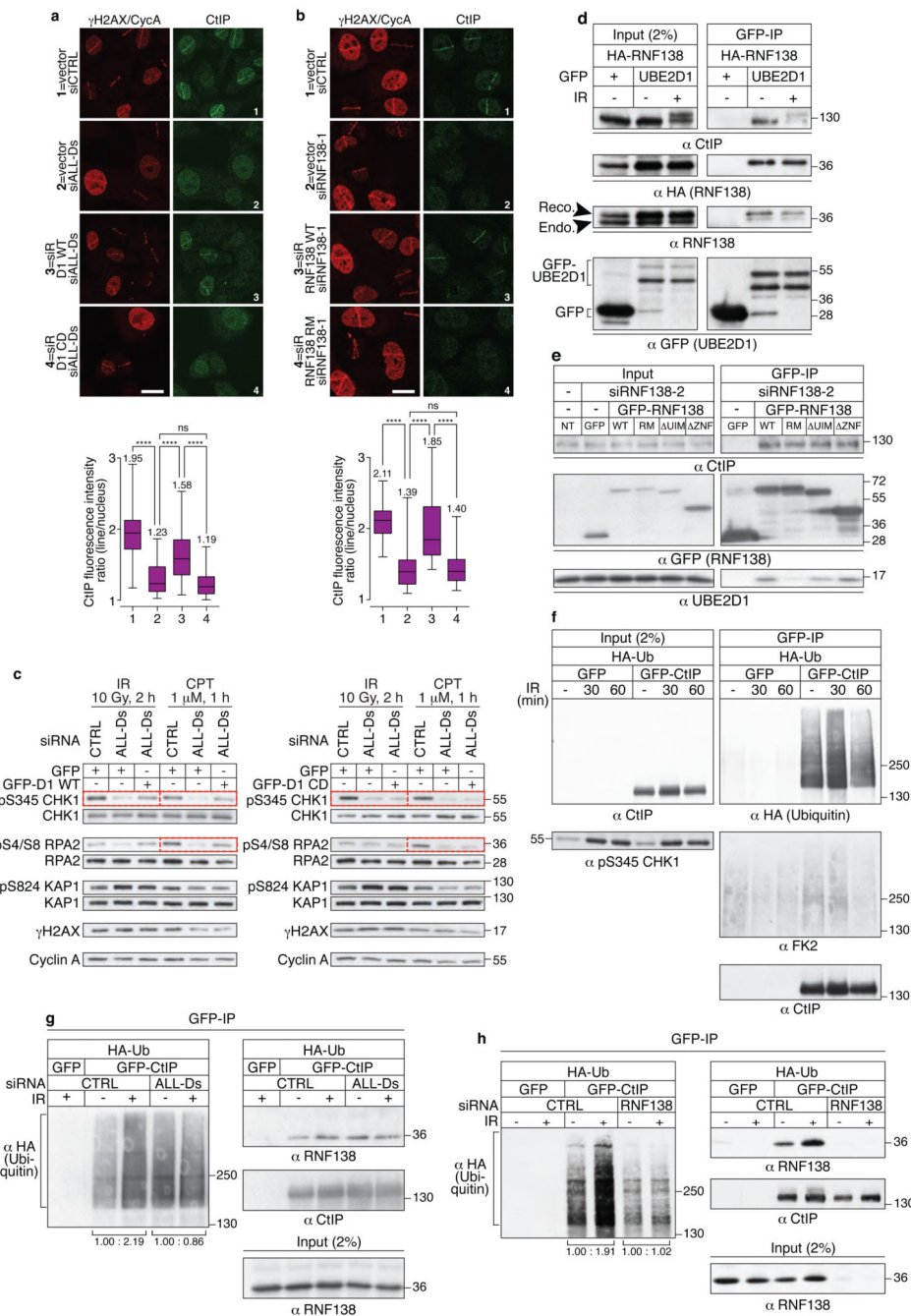
RPA2, and n=249 (siCTRL) and 173 (siALL-Ds) γH2AX-positive cells for BrdU, accumulated over two independent experiments. P-values are based on Mann-Whitney analyses. **b**, Semi-automated Opera/Acapella resection screen for selected UBE2D-interacting E3s. Negative control siRNA (siCTRL) and positive controls are highlighted in red and blue, respectively. Plot represents image field medians (lines in boxes), 25-75 percentiles (boxes) and 10-90 percentiles (whiskers) of, on average, n=203 cells per condition based on one screening experiment (only nuclei with strong γH2AX staining (yellow outlines) were selected. **c,** Defects in CPT-induced RPA2 foci and ssDNA-generation (BrdU) in siRNF138-treated cells. Dotted outlines represent nuclei according to DAPI staining. Quantifications were performed in nuclei showing strong γH2AX staining (see arrowheads), representing actively replicating S phase cells that encountered CPT-trapped TopI. Negative control siRNA (siCTRL) is shown in grey. Plots represent RPA2 or BrdU fluorescence intensity medians (lines in boxes; numbers above whiskers), 25-75 percentiles (boxes) and overall ranges (whiskers) of n=73 (siCTRL), n=74 (siRNF138-1), n=72 (siRNF138-2) γH2AX positive cells for RPA2, and n=72 (siCTRL, siRNF138-1 and siRNF138-2) γH2AX positive cells for BrdU, accumulated over two independent experiments. P-values are based on Mann-Whitney analyses. All scale bars=10 μm.
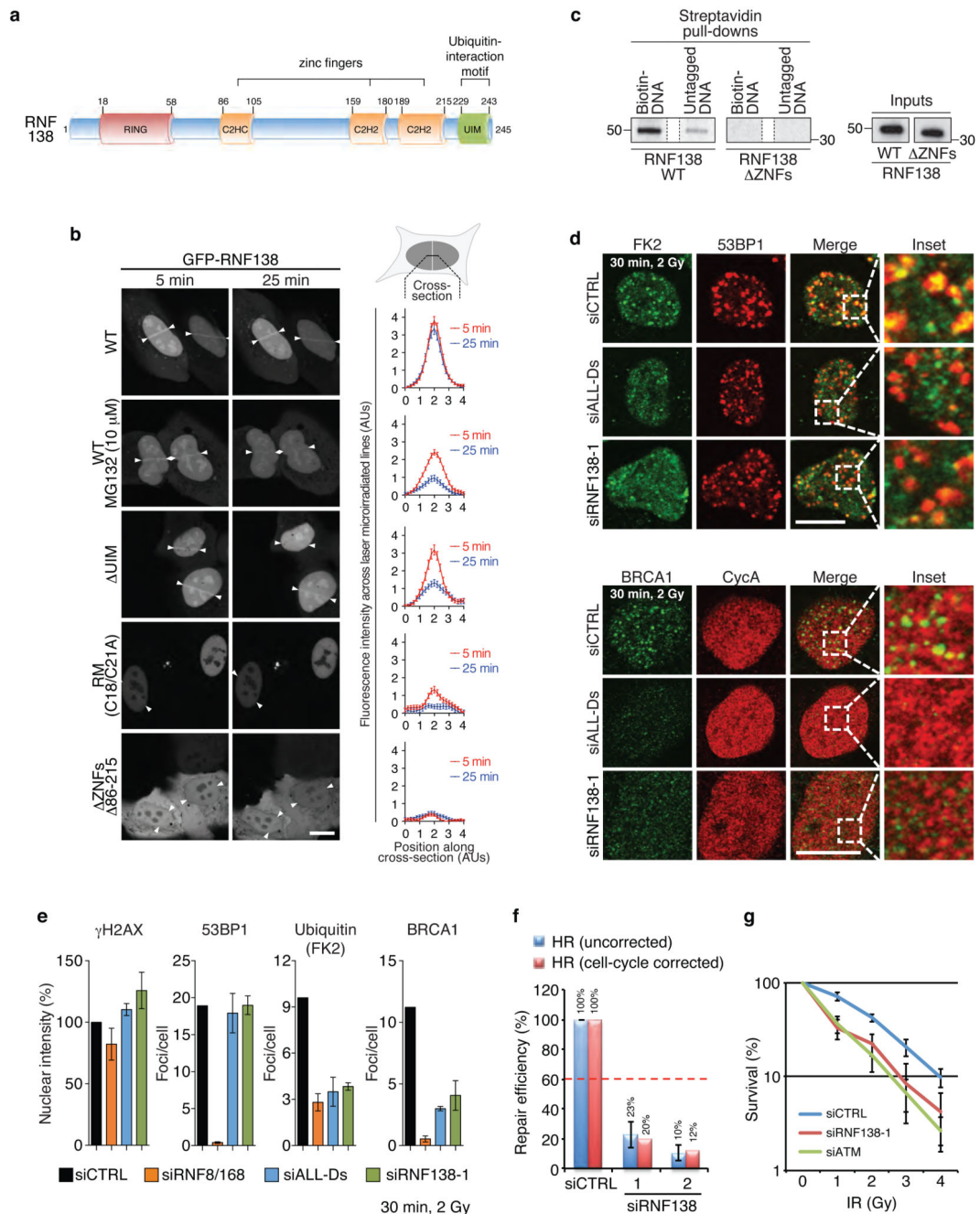
Figure 6. Phenotypic mimicry between UBE2Ds and RNF138.

a, Schematic of RNF138 domain architecture. **b,** Laser micro-irradiation experiments to determine accrual/retention requirements of siRNA-resistant GFP-RNF138 transiently expressed in U2OS cells depleted for endogenous RNF138. Data represent fluorescence intensity means of, on average, n=24 measurements ± SEM based on three measured sites across each laser tract accumulated over two independent experiments. **c,** Streptavidin pull-down experiments of biotinylated DNA in the presence of RNF138-WT or – ZNFs. Blots with dotted lines and framed by a solid line are from the same gel and the same exposure. **d,**

Depleting UBE2Ds or RNF138 impairs FK2 and BRCA1 but not 53BP1 or γH2AX IRIF. **e,** Quantification of FK2, 53BP1 and BRCA1 IRIF and mean γH2AX nuclear intensities (Opera/Acapella platform). Data represent means ± SDs of n=5 experiments for siCTRL, siRNF8+168 and siALL-Ds and n=4 experiments for siRNF138-1 (FK2 and 53BP1 foci and γH2AX nuclear intensity) and n=4 for all siRNAs (BRCA1 foci), merged from, on average, 13,971 cells per condition. Statistics source data for this panel can be found in Supplementary Table 5. **f,** TLR results for HR efficiency in siRNF138-treated U2OS cells. Note that, as HR only occurs in S/G2, data were corrected to flow-cytometry S/G2 values. Dotted line represents arbitrary cut-off at 60%. Data represent means ± SDs for n=5 independent experiments for siCTRL and n=3 for siRNF138. Statistics source data for this panel can be found in Supplementary Table 5. **g,** Clonogenic survival assays. Data represent means ± SDs of 4 independent experiments. Statistics source data for this panel can be found in Supplementary Table 5. AUs: arbitrary units. All scale bars=10 μm.

Figure 7. UBE2Ds- and RNF138-dependent CtIP-accrual and its IR-induced ubiquitylation.
a, siALL-Ds resistant WT- but not CD-GFP-UBE2D1 partially rescues CtIP accrual defects in siALL-Ds treated Cyclin A (CycA)-positive cells. Plots represent median CtIP fluorescence intensity ratios (lines in boxes; numbers above whiskers), 25-75 percentiles (boxes) and overall ranges (whiskers) of n=151 (1), 74 (2), 154 (3) and 75 (4) Cyclin A positive cells, accumulated over two independent experiments. P-values are based on Mann-Whitney analyses. ****p<0.0001. Statistics source data for this panel can be found in Supplementary Table 5. **b,** siRNF138-1 resistant WT- but not RM-GFP-RNF138 rescues

CtIP accrual defects in siRNF138-1-treated Cyclin A (CycA)-positive cells. Plots represent median CtIP fluorescence intensity ratios (lines in boxes; numbers above whiskers), 25-75 percentiles (boxes) and overall ranges (whiskers) of n=74 (1), 80 (2), 94 (3) and 76 (4) Cyclin A positive cells, accumulated over two independent experiments. P-values are based on Mann-Whitney analyses. ****p<0.0001; ns: not significant (p 0.05). Statistics source data for this panel can be found in Supplementary Table 5. **c,** siALL-Ds resistant WT- but not CD-GFP-UBE2D1 partially rescues pCHK1 and pRPA2 induction in siALL-Ds-treated U2OS cells following IR- or camptothecin (CPT) treatment. **d,** GFP-UBE2D1 co-imunoprecipitates with CtIP and RNF138 in cells irradiated or not (30 min, 15 Gy). **e,** GFP-RNF138-RING mutant (RM) does not efficiently bind UBE2D1 in cells depleted of endogenous RNF138. Comparable levels of CtIP co-immunoprecipitate with WT GFP-RNF138 and all variants. Note that this experiment was conducted under stringent conditions (500 mM NaCl). **f,** Ubiquitylation kinetics of CtIP following IR (15 Gy) at indicated times. Note that HA-ubiquitin is detected in GFP-CtIP imunoprecipitates by HA- but not FK2-antibodies. **g,** IR-induced CtIP ubiquitylation in cells depends on UBE2Ds (30 min, 15 Gy). Note that the increase in siALL-Ds-treated cells in the absence of DNA damage is due to experimental variation rather than biological significance. **h,** IR-induced CtIP ubiquitylation in cells depends on RNF138 (30 min, 15 Gy). Molecular weight markers are in kilodaltons. Reco.: recombinant; Endo.: endogenous. Experiments shown in d-h were conducted in HEK293 cells. All scale bars=10 μm.
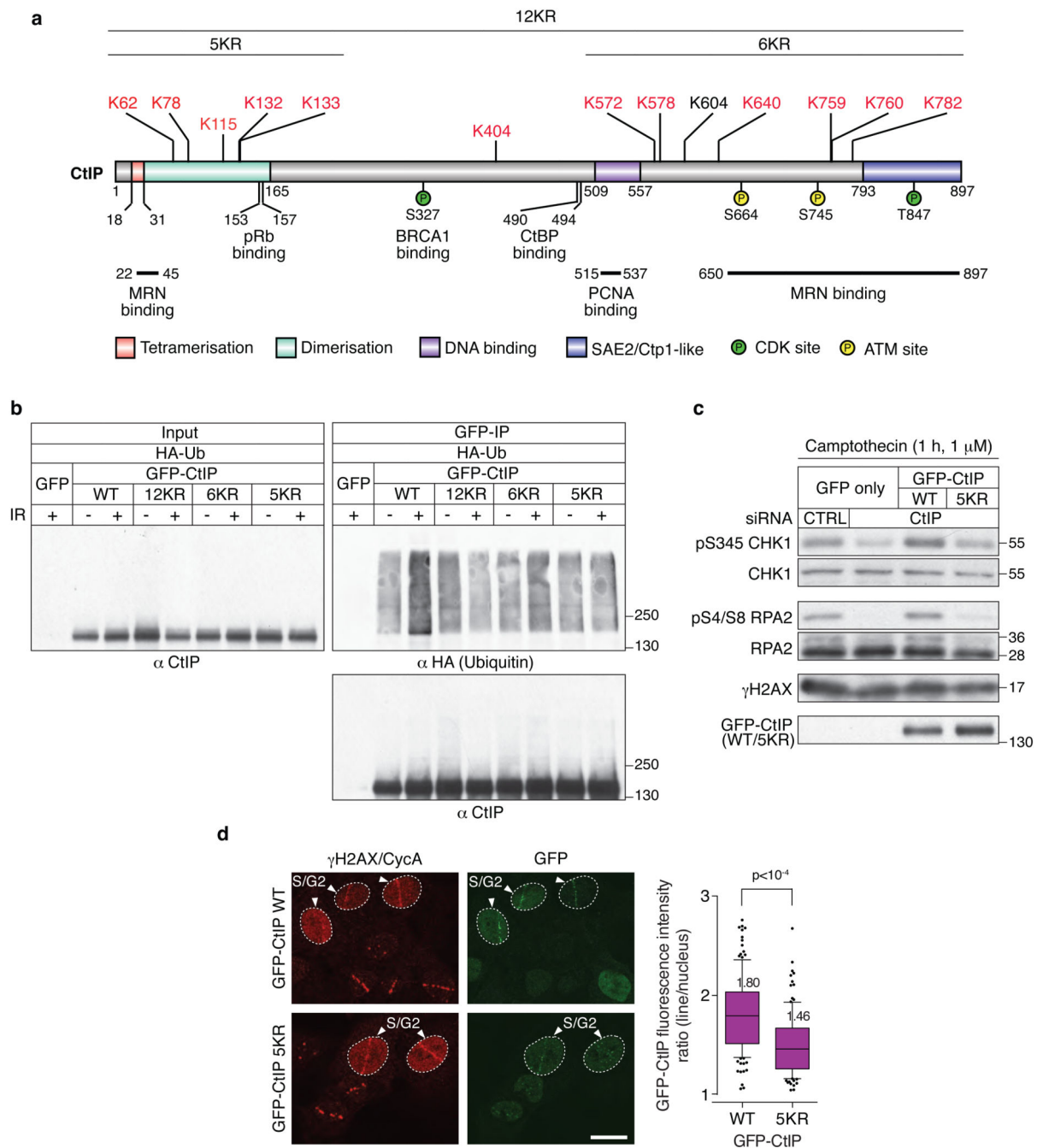
Figure 8. N-terminal, IR-induced CtIP ubiquitylation promotes its recruitment and function.
a, Schematic of CtIP showing regions/sites of interest[15,41,52]. The 13 ubiquitylated lysines (K) identified by LC-MS/MS of CtIP peptides retrieved from irradiated HEK293 cells are highlighted. K604, known to not be important for CtIP recruitment[40], is shown in black; other ubiquitylated lysines are highlighted in red. Red lysines were mutated to arginines (R), as indicated, leading to CtIP mutants 12KR, 5KR and 6KR. **b,** Defects in IR-induced CtIP ubiquitylation in HEK293 cells, especially for the CtIP-12KR and -5KR lysine to arginine mutants. **c,** siRNA-resistant GFP-CtIP-WT, but not -5KR, rescue pRPA2 and pCHK1

induction in siCtIP-treated U2OS cells, one hour after CPT-treatment. **d,** Recruitment of siRNA-resistant GFP-CtIP-5KR to sites of DNA damage induced by laser micro-irradiation in siCtIP-treated Cyclin A (CycA)-positive U2OS cells is reduced compared to wild-type GFP-CtIP. Plots represent median GFP-CtIP fluorescence intensity ratios (lines in boxes; numbers above boxes), 25-75 percentiles (boxes) and 10-90 percentiles (whiskers) of n=135 (WT) and 112 (5KR) Cyclin A positive cells, accumulated over two independent experiments. Dots represent remaining values outside 10-90 percentile. P-values are based on Mann-Whitney analyses. Scale bar=10 μm. Statistics source data for this panel are available in Supplementary Table 5. Molecular weight markers are in kilodaltons.